#### RESEARCH Open Access



# Programmable macrophage-polarizing nanoparticles for MRI-guided early detection and treatment of pulmonary metastases

Meiju Sui<sup>1,2</sup>, Kairu Xie<sup>1,2</sup>, Yingying Luo<sup>1,2</sup>, Haiqiang Wang<sup>1,2</sup>, Hao Sheng<sup>1</sup>, Sen Yue<sup>1,2</sup>, Xiaoxun Liu<sup>1,2</sup>, Sha Li<sup>1,2</sup>, Jung Soo Suk<sup>3</sup>, Shizhen Chen<sup>1,2,4</sup>, Daigin Chen<sup>1,2,4</sup> and Xin Zhou<sup>1,2,4,4</sup>

#### **Abstract**

Metastatic lung cancer remains a leading cause of cancer-related mortality worldwide, underscoring the urgent need for early detection and intervention strategies. Current diagnostic and therapeutic methods often fall short in sensitivity and efficacy, particularly for early-stage disease. In this study, we develop  $CaCO_3$ @quercetin-Mn nanoparticles (CQM NPs) integrating dual-stage macrophage reprogramming with  $T_1$ -weighted magnetic resonance imaging (MRI) enhancement for theranostic management of pulmonary metastasis. CQM NPs exploit dynamic macrophage polarization: initial M2 polarization promotes nanoparticles accumulation in metastatic lesions, enabling detection of lesions as small as 0.11 mm, while subsequent acid/glutathione (GSH)-triggered degradation reprograms tumor-associated macrophages to antitumor M1 phenotype, suppressing metastatic growth by 81.64% and preventing circulating tumor cells (CTCs) from colonizing the lungs by 78.08%. These findings demonstrate a significant improvement in MRI sensitivity and an integrated approach to therapy, contrasting with traditional methods that separate these challenges. This "detect-to-treat" paradigm bridges the critical gap between imaging sensitivity and immunomodulatory therapy, offering a blueprint for precision nanomedicine in metastatic cancers.

Keywords Pulmonary metastasis, Magnetic resonance imaging, Macrophage polarization, Nanoplatform, Theranostic

#### Introduction

According to the latest USA cancer statistics, lung cancer accounts for substantially more deaths than any other malignancy, with a five-year relative survival rate of just 27% [1]. Metastasis is the leading cause of lung cancerrelated mortality, with metastatic lung cancer standing out for its particularly poor prognosis. Statistics from 2011 to 2017 reveal a dismal 5-year relative survival rate

of only 6% for patients with metastatic lung cancer in the United States [2, 3]. Although early detection is critical, reliable identification of submillimeter metastatic lesions remains challenging [4–6], delaying treatment and limiting therapeutic efficacy.

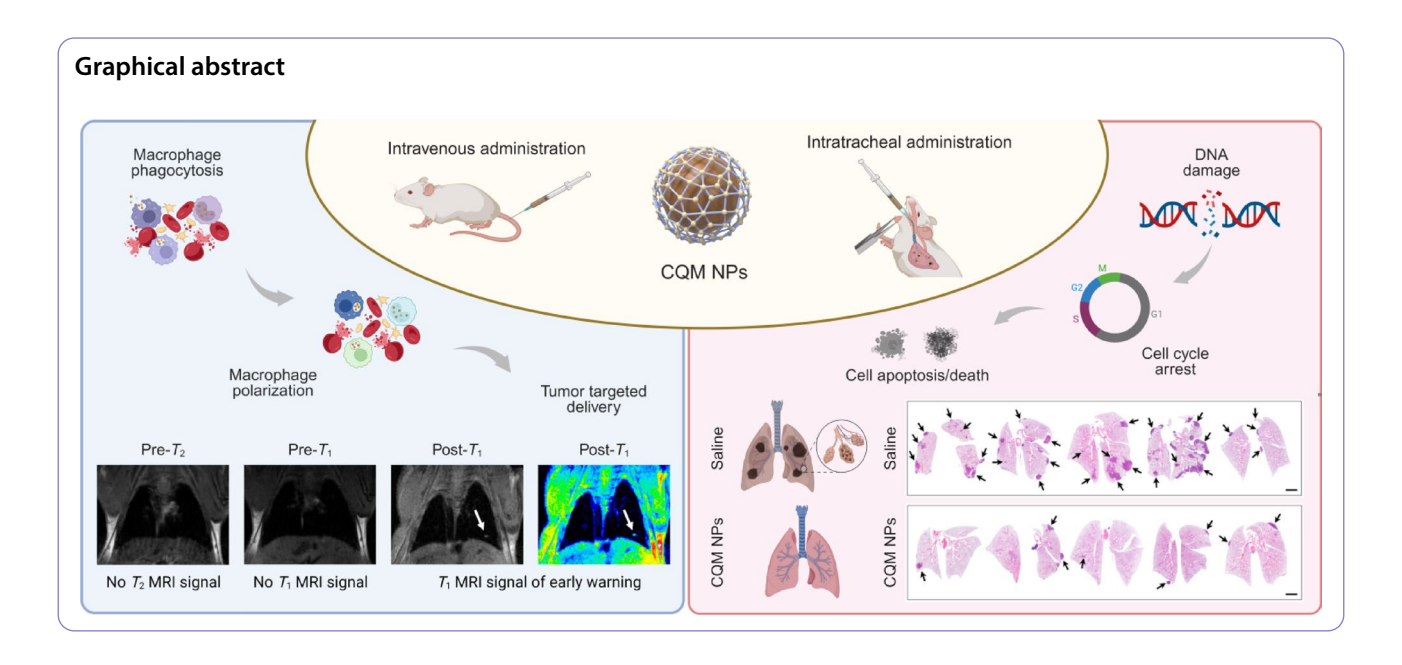
Molecular imaging, particularly MRI, has advanced the noninvasive detection of pulmonary metastases [6–11]. The benefits of MRI, including its free of ionizing radiation, deep tissue penetration, and high spatial resolution, are enhanced by contrast agents (CAs) [12–15]. However, conventional CAs struggle to detect ultra-small lesions and lack therapeutic capacity, underscoring the need for multifunctional agents that can both diagnose and treat metastases [5, 16].

\*Correspondence: Daiqin Chen chendychin@apm.ac.cn Xin Zhou xinzhou@wipm.ac.cn

Full list of author information is available at the end of the article



© The Author(s) 2025. **Open Access** This article is licensed under a Creative Commons Attribution-NonCommercial-NoDerivatives 4.0 International License, which permits any non-commercial use, sharing, distribution and reproduction in any medium or format, as long as you give appropriate credit to the original author(s) and the source, provide a link to the Creative Commons licence, and indicate if you modified the licensed material. You do not have permission under this licence to share adapted material derived from this article or parts of it. The images or other third party material in this article are included in the article's Creative Commons licence, unless indicated otherwise in a credit line to the material. If material is not included in the article's Creative Commons licence and your intended use is not permitted by statutory regulation or exceeds the permitted use, you will need to obtain permission directly from the copyright holder. To view a copy of this licence, visit http://creativecommons.org/licenses/by-nc-nd/4.0/.



Nanoparticles (NPs) have emerged as promising theranostic tools [17–21], yet systemic administration is hindered by rapid clearance and nonspecific macrophage uptake [22, 23]. In the tumor microenvironment (TME), macrophages play dual roles: M1 macrophages suppress tumor growth, while M2 macrophages and tumor-associated macrophages (TAMs) promote metastasis [24–26]. Current evidence suggests that NP phagocytosis can modulate macrophage polarization, but the direction of polarization (M1 vs. M2) is highly NP-dependent [27–29]. An optimal nanoplatform should enable programmable polarization: first exploiting M2 macrophages for targeted lesion accumulation, then reprogramming them to M1 for therapeutic benefit [30–32].

To address these challenges, we designed a core-shell nanoparticle (CQM NP) composed of a quercetin-Mn (QM) shell and  $CaCO_3$  core. The QM shell functions as a  $T_1$ -weighted MRI CA [33, 34], and induces M2 polarization to guide metastatic targeting [35, 36]. Following vesicular transport to tumor sites, the acidic TME and elevated glutathione levels trigger degradation of both the QM complexes and  $CaCO_3$  nanoparticles (CNPs), releasing bioactive components (manganese ions, calcium ions, quercetin, and  $CO_2$ ) that reprogram TAMs to the tumor-suppressive M1 phenotype.

This innovative design enables the CQM NPs to achieve three critical functions: (1) MRI detection of submillimeter metastatic lesions through enhanced contrast, (2) inhibition of metastatic colony formation via targeted accumulation, and (3) therapeutic intervention through TME modulation (Scheme 1). By integrating early diagnostic capability with timely therapeutic intervention, this multifunctional nanoplatform represents a significant advancement in the proactive management

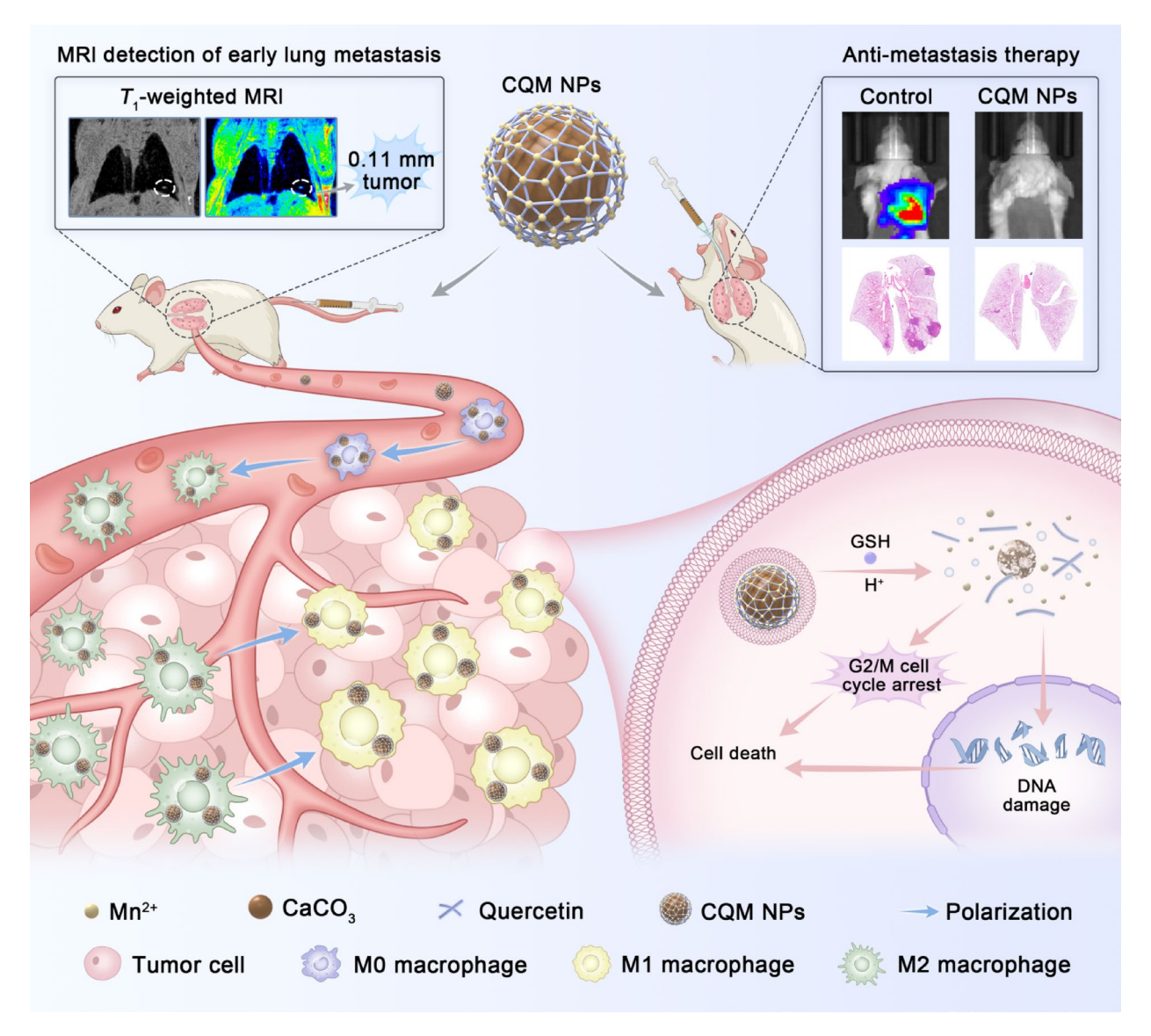
of metastatic lung cancer, offering new possibilities for combating this lethal disease.

#### **Materials and methods**

#### Materials

MnCl<sub>2</sub>·4H<sub>2</sub>O and CaCl<sub>2</sub>·2H<sub>2</sub>O were purchased from Shanghai Titan Scientific Co., Ltd. NH4HCO3 was obtained from Shanghai Aladdin Biochemical Technology Co., Ltd. Quercetin was bought from Shanghai Macklin Biochemical Co., Ltd. Ethanol, NaOH, NaH<sub>2</sub>PO<sub>4</sub>·2H<sub>2</sub>O, and Na<sub>2</sub>HPO<sub>4</sub>·12H<sub>2</sub>O were purchased from Sinopharm Chemical Reagent Co., Ltd. Reduced GSH was bought from Sigma-Aldrich Trading Co., Ltd. 3,3',5,5'-tetramethylbenzidine (TMB) was purchased from Aladdin Bio-Chem Technology Co., Ltd. 5,5'-dithiobis(2-nitrobenzoic acid) (DTNB) was purchased from Bide Pharmatech Ltd. Sulfo-Cyanine5 (Cy5) was obtained from MedChemExpress (USA). D-Luciferin potassium salt was bought from Solarbio Science & Technology Co., Ltd. Phosphate-buffered saline (PBS) was obtained from HyClone (USA). Trypsin, RPMI Medium 1640 basic (1X), Dulbecco's Modified Eagle Medium (DMEM), and fetal bovine serum (FBS) were purchased from Thermo Fisher Biochemical Products Co., Ltd. 4% neutral paraformaldehyde solution and penicillin-streptomycin (Pen-Strep) were obtained from Beijing Labgic Technology Co., Ltd. Puromycin was bought from Solarbio Science & Technology Co., Ltd. BCECF-AM and DNA Damage Assay Kit by yH2AX Immunofluorescence were obtained from Beyotime Biotechnology Co., Ltd. CellTrace Violet (Invitrogen, C34557) and CellTrace CFSE (Invitrogen, C34554) were purchased from Thermo Fisher Scientific (USA). Anti-Mo F4/80 (eFluor 450), Anti-Mo CD86 (PE-Cyanine7), and Anti-Mo CD206

Sui et al. Journal of Nanobiotechnology (2025) 23:675 Page 3 of 21



**Scheme 1** Schematic illustration of programmable macrophage-polarizing CQM NPs for MRI-guided early detection and treatment of pulmonary metastases

(APC) were obtained from Thermo Fisher Scientific (Ann Arbor, MI, USA). 4,6-diamidino-2-phenylindole (DAPI) and Cell Counting Kit-8 (CCK-8) Assay Kit were purchased from Beyotime Biotechnology Co., Ltd. Antifade solution was obtained from Boster Biological Technology Co., Ltd.

#### Synthesis of CNPs

0.6 g of  $CaCl_2 \cdot 2H_2O$  was dissolved in 400 mL of ethanol in a beaker covered with aluminum foil pierced with pores. The beaker was placed in a vacuum environment containing 10 g of  $NH_4HCO_3$  for 24 h at 30 °C. After the reaction was completed, the resulting CNPs were centrifuged at 8000 rpm and washed three times with ethanol before being redispersed in ethanol for further use.

#### Synthesis of CQM NPs

CNPs (7 mg·mL<sup>-1</sup>, 1 mL) were dispersed in 197 mL of ethanol. The reaction solution was continuously stirred at 800 rpm while 1 mL of quercetin solution (8 mM in ethanol) was added at a controlled rate of 0.01–0.05 mL/s. Under real-time monitoring with a pH meter, the pH was adjusted to 8.0 by dropwise addition of NaOH solution (0.1 M). Subsequently, 1 mL of MnCl<sub>2</sub>·4H<sub>2</sub>O solution (40 mM in ethanol) was introduced at the same rate (0.01–0.05 mL/s). The reaction was adjusted to 8.0 by NaOH solution (0.1 M) again and stirred overnight at room temperature with continuous stirring at 800 rpm. The resulting suspension was then centrifuged at 15,000 rpm for 20 min, followed by repeated washing with deionized water until the supernatant became clear. The resulting

CQM NPs were redispersed in deionized water and stored at -4 °C for future use.

# Elemental mapping of CQM NPs using energy-dispersive X-ray spectroscopy (EDS) coupled with transmission electron microscopy (TEM)

Elemental mapping of CQM NPs was conducted using energy-dispersive X-ray spectroscopy (EDS) coupled with TEM. The CQM NPs were ultrasonically dispersed in absolute ethanol (5 min, 40 kHz) and deposited onto copper grids. After vacuum drying at 25 °C overnight, the grids were loaded into a field emission transmission electron microscope (FETEM) equipped with an energydispersive X-ray spectrometer (EDS) detector to visualize the elemental distribution of C, O, Ca, and Mn in CQM NPs. Prior to mapping, the microscope was calibrated using a copper standard (Cu Kα at 8.04 keV) and operated at 200 kV with probe current stabilized at 0.5 nA to balance spatial resolution and elemental sensitivity. HAADF-STEM imaging initially identified individual CQM NPs, whereafter EDS spectral maps were acquired. For quantitative analysis, characteristic X-ray lines were selected as follows: C Kα (277 eV), O Kα (525 eV), Ca  $L\alpha$  (341 eV), and Mn  $L\alpha$  (637 eV) with respective energy windows set to  $\pm 10$  eV to exclude overlapping signals. The final elemental distribution profiles were displayed in false color. Post-processing included background subtraction using Cliff-Lorimer correction and quantitative elemental distribution analysis via Bruker Esprit software (v2.1). The overlapping signals between Ca L $\alpha$  and Mn L $\alpha$ peaks were deconvoluted through Gaussian fitting, and the atomic percentages were normalized to the sum of detected elements excluding copper from the grid.

#### Measurements of Quercetin in CQM NPs

Ethanol solutions containing quercetin at different concentrations were prepared, and their absorbance at 256 nm was measured. A standard curve of absorbance versus concentration was established using these measurements. The content of quercetin in CQM NPs was then calculated based on this standard curve.

## Measurements of manganese and calcium contents in CQM NPs by inductively coupled plasma mass spectrometer (ICP-MS)

 $200~\mu L$  of CQM NPs solution (1  $mg\cdot mL^{-1})$  was fully dissociated in 5 mL of concentrated nitric acid (HNO $_3$ ) at 70 °C for 24 h. Subsequently, the mixture solution was volatilized at 150 °C to remove HNO $_3$ . Finally, 5 mL of deionized water was added, and the manganese and calcium contents were determined by ICP-MS.

## The peroxidase (POD)-like activity of CQM NPs under different pH conditions

The POD-like activity of CQM NPs under different pH conditions was evaluated using TMB as the substrate in the presence of  $\rm H_2O_2$ . In detail, 10  $\rm \mu L$  of CQM NPs solution (0.8  $\rm mg\cdot mL^{-1}$ ) was added into 3 mL of 0.2 M buffer solution (pH 7.4, 6.5, and 5.5) containing 100  $\rm \mu L$  of TMB (2  $\rm mg\cdot mL^{-1}$  in dimethyl sulfoxide) and 900  $\rm \mu L$  of  $\rm H_2O_2$  (3%). The ultraviolet-visible (UV-vis) absorption spectra of oxidized TMB (oxTMB) was recorded by UV-vis spectrophotometer.

#### The glutathione peroxidase (GPx)-like activity of CQM NPs

To evaluate GPx-like activity, CQM NPs ( $C_{Mn}$ : 0.1, 0.2, 0.3, 0.4, and 0.5 mM) were respectively added to GSH solutions (10 mM, pH 6.5), followed by the addition of DTNB (6 mM, 100  $\mu$ L). Then the reaction solution was diluted 100 times, and the UV-vis absorption spectra of different reaction solutions was recorded by UV-vis spectrophotometer.

#### Cell lines and culture

4T1 and RAW264.7 cells were obtained from the Cell Bank of the Chinese Academy of Sciences (Shanghai, China). 4T1-Luc cells were purchased from Xiamen Immocell Biotechnology Co., Ltd. (Xiamen, China). 4T1 and 4T1-Luc cells were cultured in RPMI Medium 1640 basic (1X) supplemented with 10% FBS and 1% Pen-Strep, with the exception that 4T1-Luc cells were subjected to additional puromycin (0.5  $\mu g \cdot m L^{-1}$ ) for cell screening. RAW264.7 cells were cultured in DMEM containing 10% FBS and 1% Pen-Strep. All cells were cultured under stable conditions of 37 °C and 5% CO<sub>2</sub>.

#### **Animal model**

Female Balb/c mice (5–6 weeks of age) were purchased from Hubei Beiente Biotechnology Co., Ltd. and fed under specific pathogen-free (SPF) conditions.

To establish pulmonary metastasis model,  $1\times10^6$  4T1-Luc cells were injected intravenously into the tail vein of each mouse. To confirm pulmonary metastases, mice were intraperitoneally injected with D-luciferin potassium salt solution (15 mg·mL $^{-1}$ , 200  $\mu L$ ) 10 min before bioluminescence imaging (BLI). After in vivo imaging or therapeutic interventions, the metastatic lung tumors were further visualized and quantitatively analyzed by hematoxylin and eosin (H&E) staining.

## The disintegration behavior of CNPs and CQM NPs under different pH conditions

CNPs and CQM NPs were dispersed in buffer solutions at various pH values (7.4, 6.5, and 5.5) and incubated at 37 °C under continuous shaking (150 rpm). Morphological and size changes of CNPs and CQM NPs were

analyzed by transmission electron microscopy (TEM) at predetermined time points.

## The disintegration behavior of QM and CQM NPs in GSH solutions at various concentrations

QM and CQM NPs were individually incubated with GSH solutions at concentrations of 0, 1.25, and 2.50 mM at 37 °C under continuous shaking (150 rpm). Morphological and size changes of QM and CQM NPs were analyzed by TEM at predetermined time points.

## Mn ion release profiles of CQM NPs under varying pH or GSH conditions

CQM NPs were incubated with buffer solutions at varying pH values (5.5 and 6.5) or GSH solution (2.50 mM). At specific time points, 1 mL of the solution was extracted for subsequent analysis, and 1 mL of fresh buffer solution was added. The concentration of Mn ions in the extracted solution was determined by ICP-MS.

## Bio-transmission electron microscopy (Bio-TEM) of CQM NPs in 4T1 cells

4T1 cells were incubated with CQM NPs ( $C_{\rm Mn}$  = 0.1 mM) for 3 h. After incubation, 4T1 cells were washed three times with PBS, followed by being harvested via gentle scraping in fresh PBS containing protease inhibitors. The pelleted cells were fixed with 2.5% glutaraldehyde for 24 h at 4 °C. Finally, the as-prepared samples were observed by Bio-TEM.

#### The quantification of CQM NPs uptake by RAW264.7 cells

RAW264.7 cells were seeded in 6-well plates and cultured overnight. The next day, the medium was replaced with 1 mL of fresh DMEM containing CQM NPs, polystyrene@quercetin-Mn nanoparticles (PQM NPs), or  $CaCO_3$ @dopamine-Mn nanoparticles (CDM NPs) ( $C_{\rm Mn}$  = 0.1 mM). Cells were incubated with NPs for varying durations (0, 10, 20, 30, 60, 120, and 180 min). At each time point, cells were washed three times with PBS and harvested for manganese content analysis by ICP-MS.

#### Cytotoxicity assessment

4T1 cells and RAW264.7 cells were separately seeded into two 96-well cell culture plates  $(5\times10^3$  cells per well) and cultured overnight. The next day, 4T1 cells and RAW264.7 cells were incubated with varying concentrations of CQM NPs for 24 h. After incubation, the cell viability was measured using a CCK-8 assay kit.

#### Assessments of RAW264.7 cells polarization

RAW264.7 cells were seeded in 6-well plates ( $5\times10^5$  cells per well) and cultured overnight. Next day, RAW264.7 cells were treated with CQM NPs, PQM NPs, or CDM NPs ( $C_{\rm Mn}=0.1$  mM). At specified time points (0, 1, 3,

and 24 h), the cells were washed, collected, and subsequently stained with Anti-Mo F4/80 (eFluor 450), Anti-Mo CD86 (PE-Cyanine7), and Anti-Mo CD206 (APC) for flow cytometry (FCM) analysis. FCM analysis was performed in triplicate for each sample.

## Tumor-targeting delivery of CQM NPs via macrophage hitchhiking

RAW264.7 cells and 4T1 cells were separately plated into 6-well plates and cultured overnight. Next day, RAW264.7 cells and 4T1 cells were pre-stained with Dulbecco's phosphate-buffered saline (DPBS) contain-at 37 °C away from light for 30 min, respectively. Then, RAW264.7 cells were incubated with Sulfo-Cyanine 5@ CQM NPs (Cy5@CQM NPs) ( $C_{Mn} = 0.1 \text{ mM}$ ) for 1 h. After aspirating the supernatant, RAW264.7 cells were washed three times with DPBS and replenished with complete medium. Cells were harvested using a cell scraper, gently pipetted to homogeneity, then co-cultured with pre-stained 4T1 cells in 6-well plates for defined durations (0.5, 1, 2, 3, and 4 h). After coincubation, cells underwent DPBS rinsing followed by 15-min fixation with 4% paraformaldehyde at room temperature. Washed coverslips were mounted on glass slides for confocal imaging.

RAW264.7 cells and 4T1 cells were respectively plated into 6-well plates and cultured overnight. RAW264.7 cells were then divided into two groups: one group was left untreated, and the other group was pre-treated with 2-deoxy-D-glucose (2-DG) (8 mM) for 12 h to suppress phagocytosis. Both groups were incubated with Cy5@CQM NPs for 1 h, followed by triple PBS washing to remove uninternalized Cy5@CQM NPs. The harvested RAW 264.7 cells were co-cultured with 4T1 cells for specified durations (0, 0.5, 1, 2, 3, and 6 h). After carefully removing RAW264.7 cells, the remaining 4T1 cells were fixed and stained with Actin-Tracker Green (cytoskeleton) and DAPI (nucleus) for confocal laser scanning microscopy (CLSM) imaging.

#### Lysosomal escape assay

4T1 cells were co-cultured with RAW264.7 cells preloaded with Cy5@CQM NPs through 1-hour incubation. After co-incubation for varying durations (1, 2, 3, and 4 h), RAW264.7 cells were removed carefully. The remaining 4T1 cells were washed three times with PBS, followed by staining with Lyso-Tracker Green probe (50 nM, 37 °C for 15 min) and DAPI (5 min) for CLSM imaging.

#### Intracellular pH measurements

4T1 cells were seeded into confocal dishes at a density of  $5 \times 10^4$  cells per dish and cultured overnight. Next day,

4T1 cells were incubated with CQM NPs ( $C_{\rm Mn}$  = 0.1 mM) for varying durations (1, 2, 3, 4, and 5 h) prior to being stained with BCECF-AM pH-sensitive fluorescent probe (37 °C, 30 min). Finally, the intracellular pH level of 4T1 cells was observed by CLSM.

#### Intracellular DNA damage assay

4T1 cells were seeded into 6-well plate ( $1\times10^5$  cells per well) and cultured overnight. Next day, 4T1 cells were incubated with CQM NPs ( $C_{Mn}=0.1$  mM) for different durations (0, 2, 4, 6, and 8 h) prior to  $\gamma$ H2AX immunofluorescence staining. Finally, the intracellular DNA damage level of the 4T1 cells was observed by CLSM.

#### MRI contrast performance of CQM NPs in vitro

The longitudinal relaxation time  $(T_1)$  of CQM NPs samples under different pH conditions (7.4, 6.5, and 5.5) or GSH conditions (1.25, 2.50, and 5.00 mM) was measured by a 7T MRI scanner. The specific parameters were set as follows: RARE  $T_1 + T_2$  map sequence, matrix size =  $256 \times 256$ , slice thickness = 1 mm. The  $r_1$  relaxivity was determined through linear fitting of  $1/T_1$  as a function of Mn concentration.

Additionally, the  $T_1$ -weighted MR images of the corresponding CQM NPs samples were captured on a 7 T MRI scanner. The parameters for these images were set as follows: RARE- $T_1$  sequence, Repetition Time (TR) = 50.0 ms. Echo Time (TE) = 9.0 ms, rare factor = 1, number of average = 8, slice thickness = 1.0 mm, and matrix size =  $256 \times 256$ .

#### Biosafety test of CQM NPs

To assess the biosafety of CQM NPs, healthy Balb/c mice (female, 6 weeks old) were randomly divided into three groups. Mice of one group were left without any treatment. The mice of the other two groups were treated with CQM NPs ( $C_{\rm Mn}=0.5~{\rm mM}$ ) via intratracheal (i.t.) administration and intravenous (i.v.) injection, respectively. At 24 h post-treatment, these mice were euthanized, and blood samples were collected. Some of the blood samples were stabilized with an anti-clotting agent for blood routine analysis, while the rest were centrifuged at 3000 rpm for 10 min to obtain serum for blood biochemical analysis.

#### In vivo MR imaging of pulmonary metastases

After successfully establishing the pulmonary metastasis model, Balb/c mice with lung metastases were divided into three groups and intravenously injected with 200  $\mu$ L of CQM NPs solution, PQM NPs solution or CDM NPs solution (C<sub>Mn</sub> = 0.5 mM). They were then scanned by a 7T MRI scanner at 2 h post-injection. The acquisition parameters of  $T_1$ -weighted MRI images were as follows: RARE- $T_1$  sequence, TR = 400 ms, TE = 10 ms, number

of average = 4, rare factor = 1, matrix size =  $256 \times 256$ , FOV = 3 cm  $\times$  2.5 cm, slice thickness = 0.8 mm without gap, and acquisition time = 10 min 14 s 400 ms.

## Spatial transcriptomic analysis of dynamic macrophage polarization profiles

(1) Spatially barcoded nuclei preparation.

Fresh-frozen mouse lungs were cryosectioned at 10–20  $\mu m$  thickness using a Leica cryostat at –20 °C. Sections were processed with the SeekSpace Single Cell Spatial Transcriptome-seq Kit (K02501-08) to release nuclei and incorporate spatial barcodes. After two rounds of gentle washing and filtration through a 40  $\mu m$  strainer, nuclei were stained with AO/PI and counted on a Seekgene Fluorescence Cell Analyzer (M002B). The final nuclei suspension was kept on ice until library preparation.

(2) Library construction and sequencing.

We generated both single-cell RNA and spatial-bar-code libraries following the manufacturer's instructions (SeekSpace Kit K02501-08). Libraries were purified with VAHTS DNA Clean Beads (Vazyme N411), quantified on a Qubit Fluorometer (Thermo Fisher Q33226), and quality-checked on a Bio-Fragment Analyzer (Bioptic Qsep400). Paired-end (2×150 bp) sequencing was performed on an Illumina NovaSeq6000.

(3) Data processing.

We trimmed adapters and filtered low-quality bases with Fastp (v0.20.1), and assessed read quality metrics. Clean reads were processed by the SeekSpace Tool (v1.0.0) to assign spatial barcodes and evaluate library complexity. We aligned reads to the mouse reference genome (mm10, refdata-gex-mm10-2020-A) using STAR (v2.7.3a). UMI counts were extracted and imported into Seurat (v4.0.5) as a spatial object, retaining spatial coordinates in the reductions slot.

(4) Clustering and annotation.

We normalized gene counts by log-normalization, identified 2,000 highly variable genes with FindVariable-Features, and scaled all genes for dimensionality reduction. Principal component analysis (PCA) used the top 30 PCs for clustering via a graph-based approach (FindClusters). We visualized clusters with t-distributed stochastic neighbor embedding (t-SNE) and detected marker genes using FindAllMarkers (min.pct = 0.25). We annotated cell types with SingleR (v1.6.1) against standard reference datasets and custom SeekGene references.

(5) Quantification of M2 macrophage signatures.

We delineated tumor regions interactively on the Seek-Gene cloud platform. Within those regions, we scored macrophages for M2-related gene expression using AddModuleScore in Seurat, based on the M2 signature defined in the early-relapse hepatocellular carcinoma single-cell atlas [37].

## In vivo transportation of CQM NPs via macrophage hitchhiking

The mice bearing pulmonary metastases were intravenously injected with Cy5@CQM NPs solution (100  $\mu$ L, C<sub>Mn</sub> = 0.5 mM). Subsequently, at various time points post-injection (p.i.), their lungs were collected and sectioned. These sections were then stained with an F4/80 antibody for immunofluorescence and observed by CLSM.

#### Transcriptomic analysis

4T1 cells were seeded into a 6-well plate and cultured overnight. After incubation with CQM NPs ( $C_{\mathrm{Mn}}$  = 0.1 mM) for 3 h, the medium was replaced with fresh complete medium, and the cells were maintained for an additional 24-hour incubation. Cells were then trypsinized, lysed with Trizol reagent for 5 min, and flash-frozen in liquid nitrogen for RNA sequencing. Transcript abundance was quantified as transcripts per million using RSEM. Differential expression analysis was performed with DESeq2, identifying differentially expressed genes (DEGs) using thresholds of  $|\log_2(\text{Fold change})| \ge 1$  and false discovery rate (FDR) < 0.05. Functional enrichment analysis included: (1) GO and KEGG pathway analyses using ClusterProfiler (v4.8.3) (significance: FDR < 0.01). (2) GSEA of MSigDB Hallmark gene sets (50 sets) using GSEA software (significance: FDR < 0.05). Top enriched terms and pathways were visualized using R (v4.3.1). All statistical analyses employed Benjamini-Hochberg correction for multiple testing.

#### Antitumor therapy of pulmonary metastasis using i.t. Administration of CQM NPs

The mice confirmed to bear pulmonary metastases by BLI on day 8 were randomly divided into two groups and intratracheally treated with saline (100  $\mu$ L) or CQM NPs solution (100  $\mu$ L,  $C_{Mn}$  = 0.5 mM) on day 9, 12, 15, and 18, respectively. On day 21, the mice were sacrificed and the metastatic tumors in the lung were sectioned for H&E, Ki67, and  $\gamma$ H2AX staining prior to microscopic examination.

## Prophylactic effect of CQM NPs on pulmonary metastasis using i.t. Administration

On days -8, -5, and -2 before i.v. injection of 4T1-Luc cells, the mice were randomly divided into two groups and intratracheally treated with saline (100  $\mu$ L) or CQM NPs solution (100  $\mu$ L,  $C_{Mn}=0.5$  mM). Subsequently, the mice were i.v. injected with 4T1-Luc cells on day 0 and they were then euthanized on day 9 for subsequent analysis.

#### Histological examination

After the animal studies, mice with lung metastases were euthanized, and their vital organs (heart, liver, spleen, lung, and kidney), along with metastatic tumor tissues, were collected. These tissues were fixed in 4% paraformaldehyde overnight and subsequently embedded in paraffin. The metastatic tumors in the lung were sectioned for H&E, Ki67, and  $\gamma$ H2AX staining before microscopic examination.

#### Statistical analysis

Quantitative data are presented as means  $\pm$  standard error of mean (SEM). Unpaired two-tailed Student's t test was used for intergroup comparisons. One-way analysis of variance (ANOVA) was used to compare three or more groups. GraphPad Prism Version 9.0 software (GraphPad, USA) was utilized for statistical analysis and graphing. Asterisks were used to represent significant differences (n.s., no significance; \*P<0.05, \*\*P<0.01, \*\*\*P<0.001, and \*\*\*\*P<0.0001).

#### **Results**

#### Preparation and characterization of CQM NPs

We first prepared QM complexes and CNPs according to previous reports [38, 39], optimizing parameters that influence their physicochemical properties (hydrodynamic size, surface charge, and manganese content). These parameters included the addition sequence and speed of quercetin and Mn<sup>2+</sup> solution, as well as the pH of the reaction system (Table S1). Subsequently, we coated the CNPs with QM complexes to obtain CQM NPs. TEM images revealed a spherical morphology of CQM NPs with a diameter of approximately 100 nm (Fig. 1a). Element mapping results indicated a uniform distribution of calcium, manganese, and oxygen in CQM NPs, confirming the successful incorporation of CNPs and QM complexes (Fig. 1b), which are consistent with results of X-ray photoelectron spectroscopy (XPS) (Fig. S1). The manganese and calcium contents in CQM NPs were determined by ICP-MS, while the quercetin content was quantified via UV-vis absorbance at 256 nm (Fig. S2). The calculated compositions were 6.42%  $\pm$  0.77% quercetin, 4.62%  $\pm$ 0.43% manganese, and  $88.93\% \pm 1.17\%$  calcium. The ratio of metallic calcium to manganese in CQM NPs (Ca/Mn ≈ 19.2) measured by ICP-MS was slightly higher than that  $(Ca/Mn \approx 12.8, Table S2)$  obtained from TEM mapping. This discrepancy may arise from TEM Mapping's beamsample interaction constraints, resulting in incomplete detection of calcium carbonate core, whereas ICP-MS provides bulk elemental quantification.

Dynamic light scattering (DLS) was used to characterize CNPs (in ethanol), QM complexes (in water), and CQM NPs (in water), yielding sizes of 58.77 nm, 190.14 nm, and 105.71 nm, respectively (Fig. 1c). The

Sui et al. Journal of Nanobiotechnology (2025) 23:675 Page 8 of 21

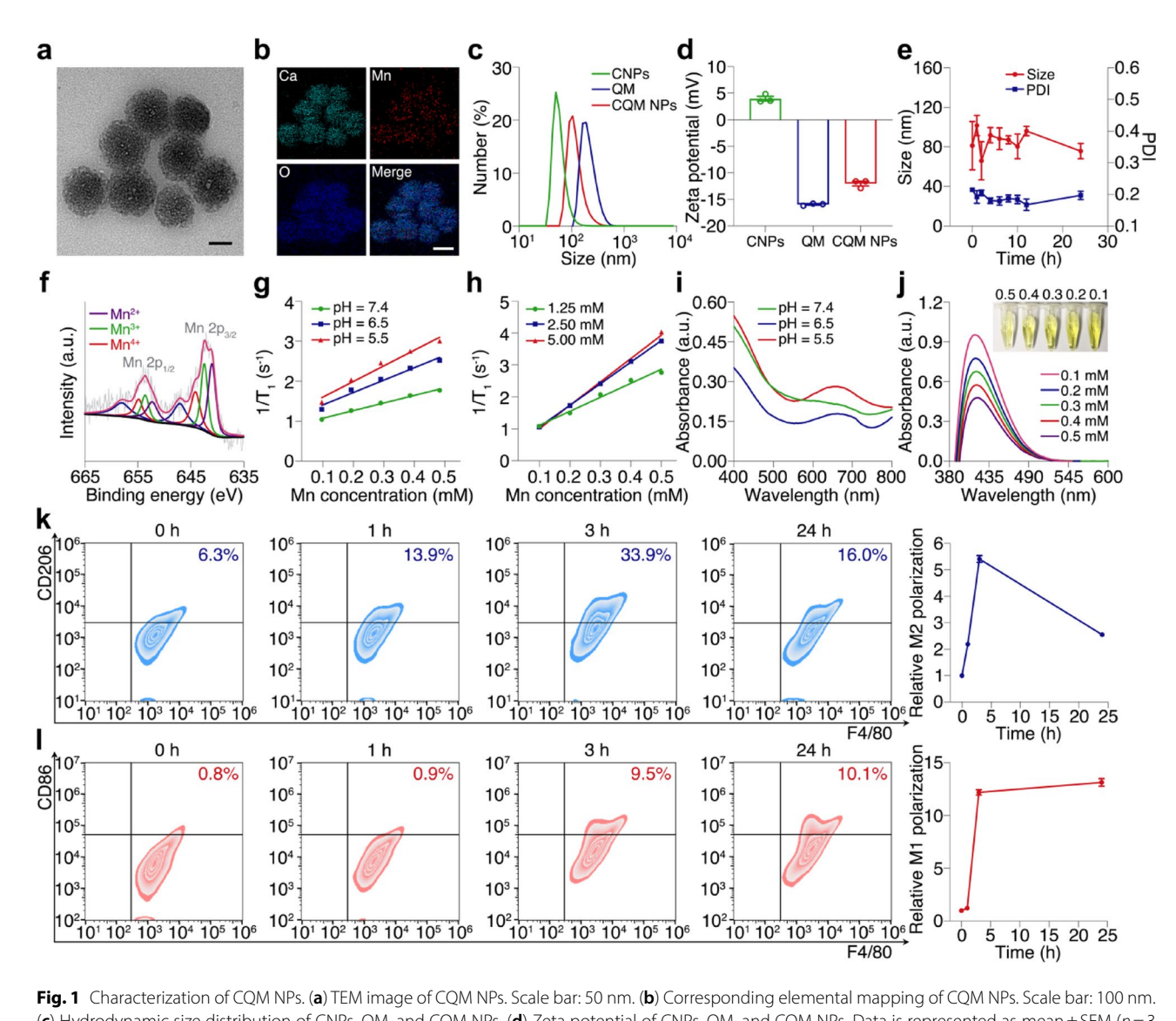


**Fig. 1** Characterization of CQM NPs. (a) TEM image of CQM NPs. Scale bar: 50 nm. (b) Corresponding elemental mapping of CQM NPs. Scale bar: 100 nm. (c) Hydrodynamic size distribution of CNPs, QM, and CQM NPs. (d) Zeta potential of CNPs, QM, and CQM NPs. Data is represented as mean  $\pm$  SEM (n=3 independent experiments). (e) Stability of CQM NPs in DMEM supplemented with 10% FBS. Data is represented as mean  $\pm$  SEM (n=3 independent experiments). (f) XPS spectra for Mn 2p region of CQM NPs, with purple, green, and red peaks representing Mn<sup>2+</sup>, Mn<sup>3+</sup>, and Mn<sup>4+</sup>, respectively. (g, h) Longitudinal relaxivity of CQM NPs under varying pH conditions (7.4, 6.5, and 5.5) (g) and GSH concentrations (1.25, 2.50, and 5.00 mM) (h). (i) UV-vis absorption spectra of TMB in the CQM NPs + H<sub>2</sub>O<sub>2</sub> reaction system across different pH values (7.4, 6.5, and 5.5). (j) UV-vis absorption spectra of DTNB in the CQM NPs + GSH reaction system at various CQM NPs concentrations, with corresponding solution photographs (inset). (k, l) FCM profiles and quantification of M2 (k) and M1 (l) polarization in RAW264.7 cells after treatment with CQM NPs over time. Data is represented as mean  $\pm$  SEM (n=3 independent experiments)

zeta potential of CNPs was measured at 3.97 mV, which shifted to –12.03 mV after coating with QM complexes (Fig. 1d). The slight increase in size and change in surface charge of CQM NPs, compared to uncoated CNPs, further support the successful coating of QM complexes. We investigated the valence state of manganese in CQM NPs using XPS. The prominent Mn 2p<sup>3/2</sup> peaks were resolved into three components at 641.3 eV, 642.3 eV, and 643.7 eV, corresponding to Mn<sup>2+</sup>, Mn<sup>3+</sup>, and Mn<sup>4+</sup>, respectively (Fig. 1e). The presence of high-valence manganese may confer glutathione (GSH) reactivity to CQM NPs.

We initially assessed the stability of CQM NPs under physiological conditions by monitoring size changes via DLS. In DMEM containing FBS, no significant changes in size or polydispersity index (PDI) were observed after 24 h of incubation, indicating high stability for subsequent studies (Fig. 1f). We then examined the responsiveness of CQM NPs to pH and GSH by observing size and morphology changes under varying conditions via TEM. The results confirmed the disintegration of the calcium carbonate core at pH 6.5, followed by the collapse of the QM coating at pH 5.5 (Fig. S3). Similarly, exposure

to GSH of different concentrations resulted in noticeable changes in size and morphology (Fig. S4).

Next, we evaluated the longitudinal relaxation properties and  $T_1$ -weighted MRI brightening performance of CQM NPs under different pH and GSH conditions. The  $T_1$ -weighted MRI performance of CQM NPs was strongly dependent on acidity, with longitudinal relaxivity values at pH 7.4, 6.5, and 5.5 measured at 1.91, 3.11, and 3.92 mM<sup>-1</sup>.s<sup>-1</sup>, respectively (Fig. 1g and S5). The contrast capability of CQM NPs positively correlated with GSH concentration (Fig. S6), yielding longitudinal relaxivity values of 4.39, 6.76, and 7.33 mM<sup>-1</sup>.s<sup>-1</sup> at GSH concentrations of 1.25, 2.50, and 5.00 mM, respectively (Fig. 1h). Given that the responsiveness of many Mnbased nanoparticles is often attributed to the release of Mn ions [40], we investigated the release profile of Mn ions under varying pH and GSH conditions. A significant release of Mn ions (31.75%) was observed after exposure to 2.50 mM GSH over 48 h, whereas only limited release occurred in acidic conditions (3.50% and 4.84% at pH 6.5 and 5.5, respectively) (Fig. S7). Thus, we attributed the responsiveness of CQM NPs' longitudinal relaxivity to changes in morphology and the release of Mn ions in response to GSH.

Numerous Mn-based nanomaterials have been developed for antitumor therapy due to their versatile enzyme-like activity [41, 42]. The presence of Mn<sup>2+</sup>, Mn3+, and Mn4+ may endow CQM NPs with POD and GPx-like activity. To assess POD-like activity, we utilized TMB as a chromogenic agent to evaluate the generation of hydroxyl radical (•OH) in the presence of H<sub>2</sub>O<sub>2</sub> and CQM NPs under different pH conditions. As illustrated in Fig. 1i, no characteristic absorbance peak of oxTMB was observed at 652 nm in the phosphate buffer solution (pH 7.4), indicating the absence of catalytic oxidation under neutral conditions. In contrast, the absorbance of oxTMB at 652 nm increased significantly as the pH decreased, demonstrating the generation of •OH catalyzed by CQM NPs under mildly acidic conditions. Since CQM NPs could only catalyze H<sub>2</sub>O<sub>2</sub> to produce •OH specifically in TME-like acidic conditions, damage to normal cells can be minimized. For the assessment of GPx-like activity, we employed DTNB (Ellman's reagent), which reacts with GSH to generate a yellow product with a maximum absorption at 412 nm. According to the results of Ellman's assay, GSH was efficiently depleted by the high-valent manganese species in CQM NPs, which was confirmed by the remarkably low absorbance of DTNB at 412 nm. The GSH consumption demonstrated a distinct dose-dependent relationship with CQM NPs (Fig. 1j).

We then assessed the polarization of inactive RAW264.7 cells after exposure to CQM NPs using FCM. A remarkable polarization to the M2 phenotype was observed within 3 h of CQM NPs treatment, with relative

M2 polarization elevated to 5.41 (Fig. 1k). Then it gradually reversed to M1 polarization from 3 h to 24 h, with relative M1 polarization was elevated to 12.18 and 13.11, respectively (Fig. 1l). To investigate the underlying mechanism of the macrophage polarization capability, we synthesized PQM NPs and CDM NPs as control NPs, each sharing the same QM shell and  ${\rm CaCO_3}$  core as CQM NPs, respectively (Fig. S8). The required programmable polarization trend was not observed in RAW 264.7 cells treated with neither PQM NPs nor CDM NPs, indicating that the core-shell components of CQM NPs synergistically mediated the sequential macrophage polarization (Fig. S9 and S10).

### MRI of ultrasmall metastatic lung tumors using CQM NPs as a CA

Before evaluating the  $T_1$ -weighted MRI brightening performance of CQM NPs in vivo, we systematically assessed their toxicity to mice via different administration routes, examining H&E staining of major organs (heart, liver, spleen, lung, and kidney) as well as conducting blood routine and biochemistry tests. All assessments indicated that the health of mice treated with CQM NPs remained within a reasonable and safe range, showing no significant differences compared to untreated controls (Fig. S11 and Table. S3 and S4).

We then scanned the lungs of mice confirmed to have metastatic lung tumors via BLI using  $T_1$ -weighted MRI. No obvious MRI signals were detected initially (Fig. 3a). Subsequently, we acquired  $T_1$ -weighted MRI images using CQM NPs as a CA, revealing clear  $T_1$ -weighted MRI signals in the lungs 2 h p.i., which were well-co-localized with pulmonary metastases identified by BLI (Fig. 2a). Notably, the MRI signals from CQM NPs accumulation at the pulmonary metastases were also well-correlated with H&E staining of the lung (Fig. 2b). Remarkably, we successfully detected tumor lesions as small as 0.11 mm using CQM NPs as a  $T_1$ -weighted CA (Fig. S12), nearly one fourth of the size of metastatic tumors detected with manganese ferrite nanoparticles in a previous study [43].

We also tested the in vivo MRI contrast capabilities of CDM NPs and PQM NPs regarding pulmonary metastases after i.v. injection to investigate the underlying mechanism of the tumor-homing capability of CQM NPs. Neither control nanoparticle showed bright  $T_1$ -weighted MRI signals in the lungs of metastases-bearing mice, indicating that the combination of the CaCO $_3$  core and QM shell in CQM NPs is essential for tumor targeting and imaging (Fig. 2a).

We evaluated the tumor-targeting capability of macrophage-mediated CQM NPs in a murine pulmonary metastasis model. Using immunofluorescence histology, we stained macrophages with F4/80 antibody (green

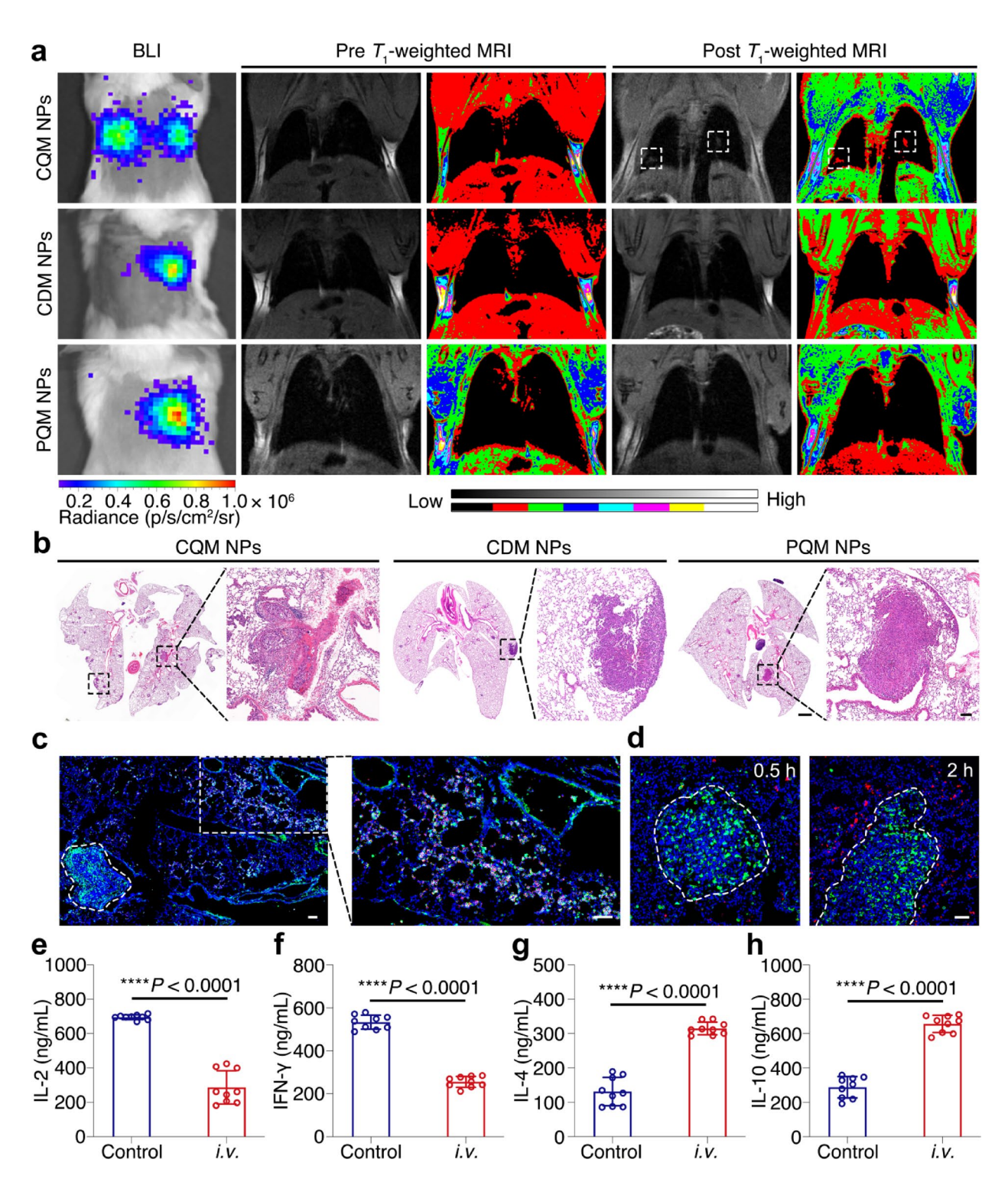


**Fig. 2** MRI of ultrasmall metastatic lung tumors using macrophage-hitchhiked CQM NPs. (**a**) BLI and  $T_1$ -weighted MRI of the lungs in pulmonary metastases-bearing mice before and after administration of CQM NPs (top panel), CDM NPs (middle panel), and PQM NPs (bottom panel). Dotted rectangles indicate locations of pulmonary metastatic lesions. (**b**) H&E staining of lungs in (**a**), scale bars for low and high magnification H&E images are 1 mm and 100 μm, respectively. (**c**) Immunofluorescence histology of lungs in pulmonary metastases-bearing mice at 30 min *p.i.* of Cy5@CQM NPs; scale bar: 100 μm. The white dashed area indicates pulmonary metastasis. (**d**) Immunofluorescence histology of lung tumors in mice at 30 min (left) and 2 h (right) *p.i.* of Cy5@CQM NPs; scale bar: 50 μm. Dashed lines indicate tumor margins. Fluorescence labels: DAPI (blue), F4/80 (green), and Cy5@CQM NPs (red). (**e**, **f**) Levels of M1-related cytokines (IL-2 (**e**) and IFN-γ (**f**)) in bronchoalveolar lavage fluid (BALF) from pulmonary metastases-bearing mice following CQM NPs treatments. Data is represented as mean ± SEM (n = 9 independent experiments).

fluorescence) and labeled COM NPs with cyanine-5 (Cy5@CQM NPs, red fluorescence). Our findings confirmed that fluorescence labeling did not significantly alter the key physicochemical properties of CQM NPs, such as hydrodynamic size and zeta potential (Fig. S13), thereby excluding the possibility that labeling-induced alterations could affect their in vivo performance. At 30 min p.i., most red fluorescence was located away from the pulmonary metastatic tumors (co-localized areas of dense blue and green fluorescence) and showed high colocalization with green fluorescence, indicating that macrophages had successfully phagocytosed the CQM NPs (Fig. 2c). At 2 h p.i., the red and green fluorescence became spatially separated, with the red fluorescence significantly localized near tumor sites, suggesting effective CQM NPs transport to tumor sites mediated by macrophages (Fig. 2d).

Since macrophages exhibit distinct M1 and M2 activation states, we further investigated macrophage polarization during the "hitchhiking" process by measuring M1-related (IL-2 and IFN-γ) and M2-related (IL-4 and IL-10) cytokines [44] of CQM NPs-treated metastasesbearing mice. Levels of IL-2 and IFN-γ decreased by 58.72% and 52.12%, respectively (Fig. 2e, f), while IL-4 and IL-10 increased 1.40- and 1.28-fold, respectively, showing a marked shift toward an M2 phenotype (Fig. 2g, h).

We also used spatial transcriptomics to track macrophage polarization within and around pulmonary metastatic tumors (Fig. 3a-c). Notably, M2-related gene expression in metastatic tumor sites was 1.78-fold to baseline at 3 h *p.i.* of CQM NPs, indicating that CQM NPs treatment effectively promoted in vivo M2 polarization (Fig. 3d). All these results collectively indicate that CQM NPs can induce macrophages towards M2 phenotype after phagocytosis, which enhances their selective accumulation in the tumor sites.

## Macrophage-mediated intercellular transport mechanism of CQM NPs

To explore whether macrophages could deliver hitch-hiked CQM NPs to tumor cells, we monitored their intercellular trafficking between RAW264.7 cells and 4T1 cells. First, we established the safe concentration range of CQM NPs for RAW264.7 cells as 6.25–150  $\mu M$  (Fig. S14), with phagocytosis peaking at 1 h post-incubation (Fig. S15). For subsequent experiments, RAW264.7 cells were pre-stained and incubated with Cy5@CQM NPs for 1 h to achieve saturation, then co-cultured with green-fluorescent-labeled 4T1 cells. Their interactions were dynamically tracked using CLSM (Fig. 4a). Initially, the red fluorescence was almost exclusively localized within RAW264.7 cells. Strikingly, the red-green fluorescence overlap (indicated by white arrows) increased

progressively, peaking at 3 h post-treatment, demonstrating efficient CQM NPs transport from RAW264.7 cells to 4T1 cells (Fig. 4b). Notably, we observed small vesicles containing Cy5@CQM NPs budding from the macrophage membrane, suggesting successful exocytosis (Fig. 4b). After 2 h incubation, while abundant Cy5@ CQM NPs remained in macrophage-derived vesicles, clear colocalization with 4T1 cells was evident (Fig. 4b and S16), indicating vesicle-mediated NPs translocation. To unequivocally verify this mechanism, we isolated macrophage-derived vesicles via centrifugation and observed substantial CQM NPs accumulation within them, as evidenced by strong red-blue fluorescence colocalization (Fig. 4c). Furthermore, when we inhibited Cy5@CQM NPs phagocytosis using 2-DG (a potent endocytosis blocker), 4T1 cell uptake decreased by 4-fold (Fig. 4d, e). This stark reduction underscores the indispensable role of macrophage hitchhiking in tumor-targeted NP delivery.

Using  $T_1$ -weighted MRI, we assessed 4T1 cells after co-incubation with RAW264.7 cells, which had prephagocytized CQM NPs. The  $T_1$ -weighted MRI images of 4T1 cells demonstrated a dose-dependent  $T_1$  contrast effect, semi-quantitatively reflecting CQM NPs delivery to tumor cells via RAW264.7 cells (Fig. 4f). Additionally, ICP-MS measurements of cytosolic Mn content in 4T1 cells post-macrophage delivery of CQM NPs, PQM NPs and CDM NPs showed comparable Mn uptake for CQM NPs and CDM NPs, while PQM NPs led to negligible uptake, suggesting that macrophage-mediated delivery is largely driven by the CaCO $_3$  core rather than the QM coating (Fig. S17).

## Mechanism investigation of the antitumor efficacy of macrophage-hitchhiked CQM NPs

Given our earlier observations of potential reversal polarization to M1 phenotype after transcytosis to cancer cells (Fig. 11), we tracked the fate of COM NPs in 4T1 cells and investigated their antitumor efficacy. We performed CLSM with lysosome labeling, showing initial localization in lysosomes followed by cytoplasmic release. Notably, a reduction in lysosomal green fluorescence, which suggests lysosomal membrane permeabilization, was observed 4 h post-treatment, indicating significant cytotoxic effects on 4T1 cells (Fig. S18). Furthermore, TEM images demonstrated that following internalization by 4T1 tumor cells, the CaCO<sub>3</sub> core of CQM NPs undergoes disintegration within lysosomes, accompanied by the emergence of CO<sub>2</sub> bubbles (Fig. 4g). Given CQM NPs would disintegrate to generate CO2 after reaction with H<sup>+</sup> in the acidic lysosomal environment, we used a pH probe (BCECF-AM, green fluorescence) to track intracellular pH changes. Strong and time-dependent green fluorescence in 4T1 cells indicated elevated intracellular

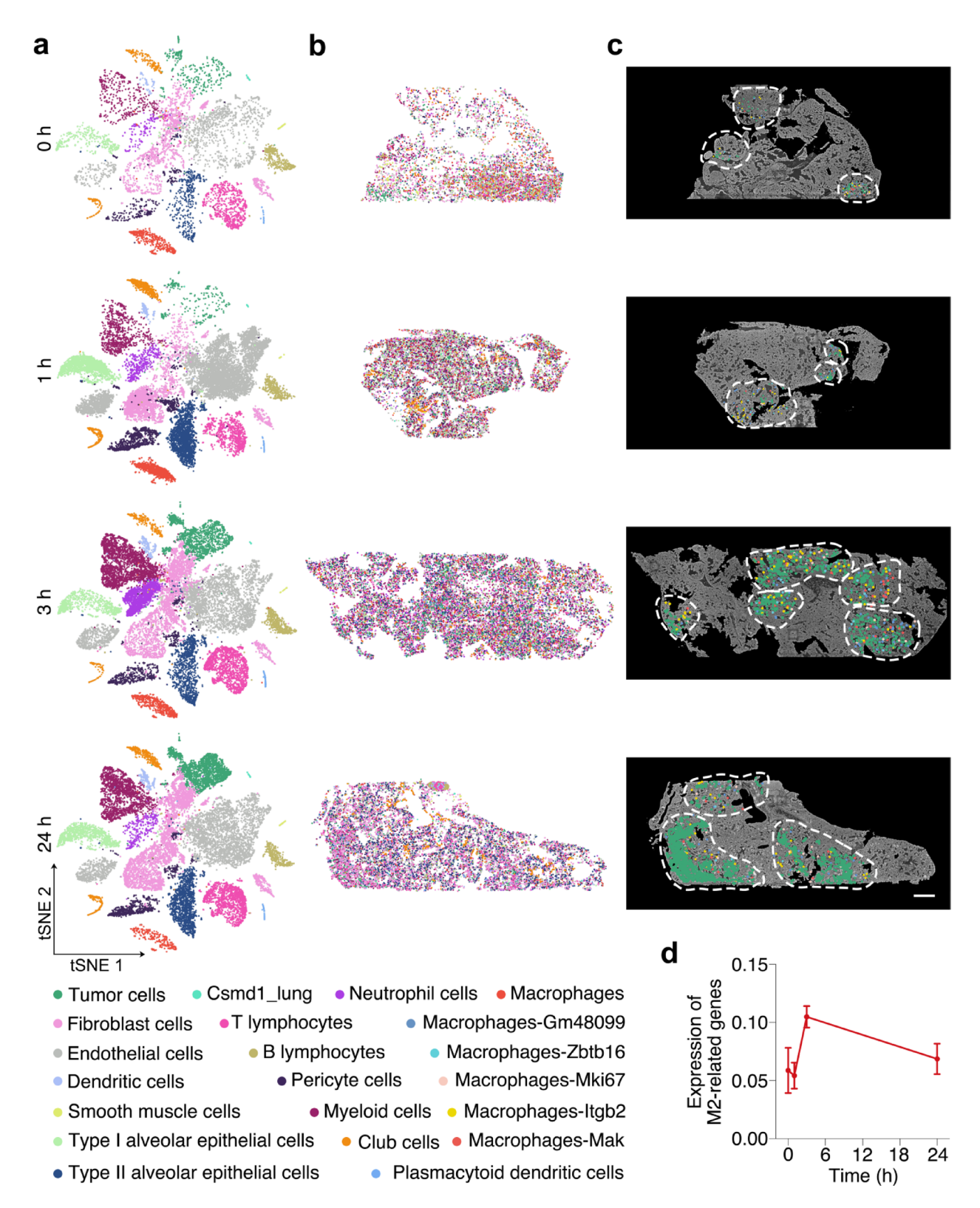


**Fig. 3** Spatial transcriptomics analysis of macrophage polarization within and around pulmonary metastatic tumors. (a) tSNE plots showing annotated cell types per sample. (b) The spatial distribution of annotated cell types in each sample. (c) The cell mapping of the lung by spatial transcriptome assay at different time points (0, 1, 3, and 24 h). The scale bar represents 1 mm. The dashed areas indicate the presence of pulmonary metastases. (d) In vivo M2 polarization of macrophages in the lungs of pulmonary metastases-bearing mice at various time points p.i. of CQM NPs, as assessed by spatial transcriptome analysis. Data is represented as mean  $\pm$  SEM (n=3 or 5)

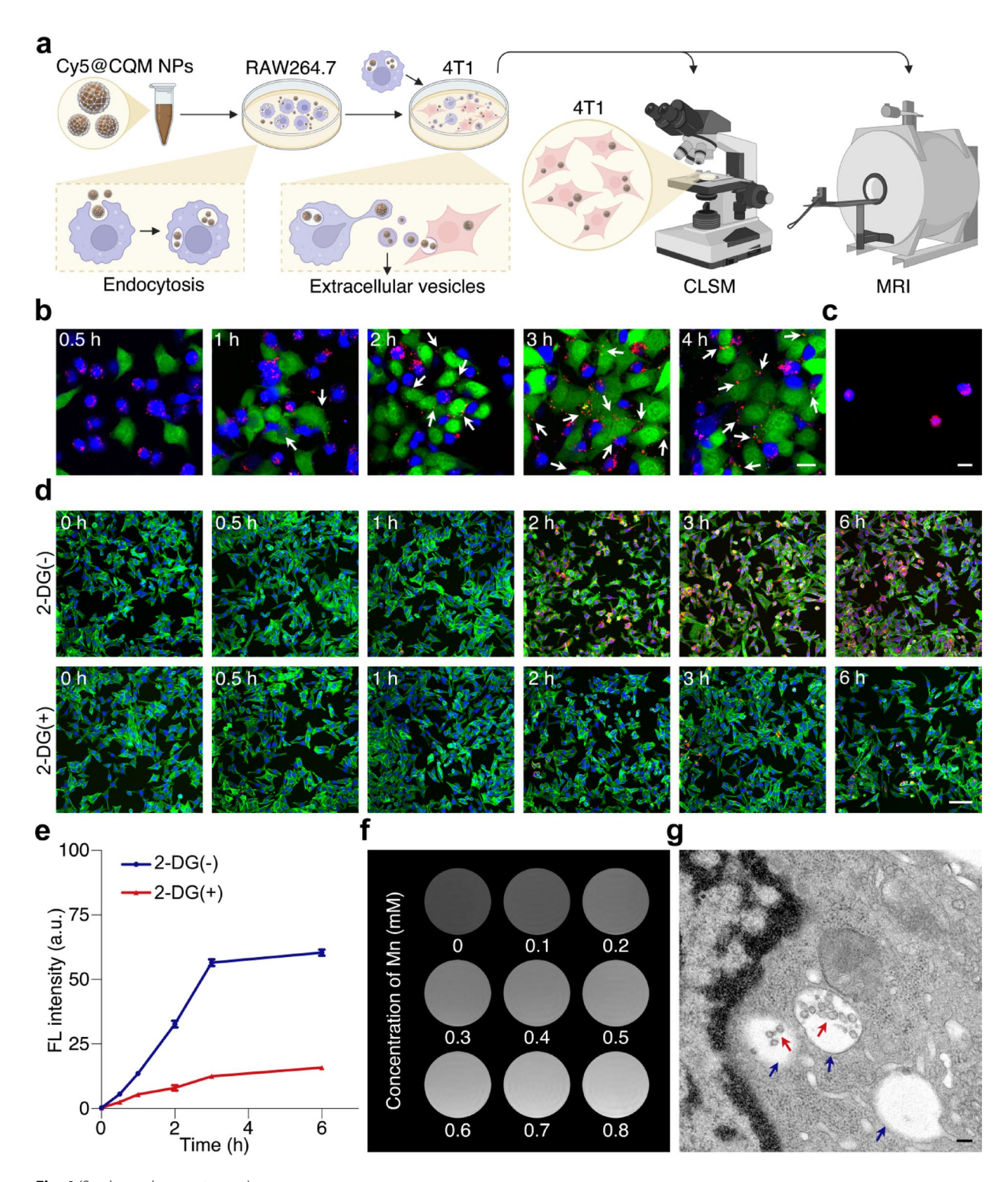


Fig. 4 (See legend on next page.)

pH levels following CQM NPs incubation (Fig. S19). Additionally,  $\gamma$ H2AX staining (green fluorescence) revealed DNA damage in 4T1 cells post-CQM NPs treatment, consistent with reports of Mn-based NP-induced DNA damage in tumor cells [45, 46]. The green fluorescence intensity increased with extended incubation time,

indicating that CQM NPs effectively induced DNA damage within 4T1 cells (Fig. S20). Collectively, these findings prompted us to evaluate the antitumor efficacy of macrophage-hitchhiked CQM NPs. Results showed that CQM NPs exhibited a dose-dependent inhibition behavior on 4T1 cell viability, with a significant 53.16% viability

(See figure on previous page.)

**Fig. 4** Mechanism of cancer cell targeting by CQM NPs via macrophage hitchhiking. (a) Schematic representation of cellular studies illustrating the transport route of CQM NPs to cancer cells facilitated by macrophage hitchhiking. (b) CLSM images of vesicle-mediated delivery from RAW264.7 cells to 4T1 cells, shown at various time points. Fluorescence labels: RAW264.7 cells and their extracellular vesicles (blue), 4T1 cells (green), and Cy5@CQM NPs (red); scale bar: 20 μm. The white arrows indicate CQM NPs successfully delivered into 4T1 cells. (c) CLSM image of extracellular vesicles secreted by RAW264.7 cells in the supernatant. Fluorescence labels: extracellular vesicle (blue) and Cy5@CQM NPs (red); scale bar: 10 μm. (d) CLSM images of 4T1 cells after incubation with RAW264.7 cells that were first treated with 2-DG for 12 h, followed by incubation with Cy5@CQM NPs for 1 h, with macrophages subsequently removed at different time points. Fluorescence labels: DAPI (blue), actin tracker (green), and Cy5@CQM NPs (red); scale bar: 100 μm. (e) Quantification of mean fluorescence intensity of Cy5@CQM NPs in 4T1 cells across different time points. 4T1 cells were co-incubated with RAW264.7 cells that were pre-treated with or without the phagocytosis inhibitor 2-DG before exposure to Cy5@CQM NPs. Data is represented as mean ± SEM (n = 3 independent experiments). (f)T<sub>1</sub>-weighted MRI image of 4T1 cells after incubation with RAW264.7 cells pre-treated with varying concentrations of CQM NPs. (g) Bio-TEM image of 4T1 cells following incubation with RAW264.7 cells pre-treated with CQM NPs; scale bar: 100 nm. Red and blue arrows highlight the presence of CQM NPs and air bubbles, respectively

loss at a concentration of 150 µM CQM NPs (Fig. S21). Additionally, we performed transcriptomic analysis to dissect the antitumor mechanisms of CQM NPs. A total of 3,724 DEGs were identified following treatment with CQM NPs, including 2,120 significantly upregulated and 1,604 significantly downregulated genes (Fig. 5a). Gene Ontology (GO) enrichment analysis of these DEGs revealed that DNA damage-related terms, including DNA replication in biological processes (BP), several chromosome-associated terms in cellular components (CC), and helicase activity in molecular functions (MF), were significantly enriched (Fig. 5b). For Kyoto Encyclopedia of Genes and Genomes (KEGG) enrichment analysis, DNA damage-related pathways such as DNA replication, mismatch repair, and base excision repair were also significantly enriched (Fig. 5c). These findings were consistent with the yH2AX staining results, which demonstrated that CQM NPs induced DNA damage in 4T1 cells. To further characterize pathway-level alterations across cancer hallmarks, we conducted Gene Set Enrichment Analysis (GSEA) using 50 Hallmark pathways. Consistently, the DNA damage-responsive pathway-UV response down was significantly enriched in CQM NPs-treated 4T1 cells. Concurrently, inflammatory signaling pathways, including TNF-α signaling via NF- $\kappa$ B, IFN- $\alpha/\gamma$  response, and inflammatory response, exhibited significant enrichment in CQM NPs treated 4T1 cells, reflecting the CQM NPs' ability to trigger protumoricidal immune and inflammatory cascades. Conversely, proliferation-associated pathways critical for cell cycle progression (e.g., G2M checkpoint and E2F targets) were significantly enriched in control cells. Notably, the enrichment of oxidative phosphorylation pathway in control cells suggested potential metabolic reprogramming toward energy stress triggered by treatment with CQM NPs (Fig. 5d). The enrichment plots and top 5 DEGs of representative pathways are displayed in Fig. 5e, f and S22. These integrated findings collectively highlight multi-modal effects of CQM NPs inducing DNA damage, activation of inflammation responses, and inhibition of proliferation and metabolic adaptation in cancer cells.

## Antitumor therapy of pulmonary metastasis using i.t. Administration of CQM NPs

We then investigated CQM NPs' potential as a therapeutic candidate for pulmonary metastasis. Unlike metastasis detection, which prioritizes an optimal tumor-to-background ratio (TBR), effective anti-metastasis treatment requires maximum accumulation of CQM NPs in lung lesions with minimal off-target exposure to achieve potent therapeutic outcomes while minimizing potential side effects. Compared to *i.v.* administration, local pulmonary delivery resulted in over a 10-fold increase in CQM NPs accumulation in lung lesions, along with significantly reduced blood levels, making it a promising approach for pulmonary anti-metastasis treatment (Fig. S23 and S24).

Prior to anti-metastasis treatment, we tracked pulmonary metastasis development using BLI in the murine model following i.v. injection of 4T1-Luc cells. Strong bioluminescent signals from the lungs were observed on day 9, confirming the successful establishment of pulmonary metastasis. The mice with lung metastases were then randomly assigned to two groups: one receiving CQM NPs (experimental group) and the other saline (control group), with treatments administered every three days starting from day 9. The animals were sacrificed on day 21 for H&E analysis following BLI assessment (Fig. 6a). Following four anti-metastasis treatments, the control group exhibited much stronger lung bioluminescence than the CQM NPs-treated group, with total bioluminescence intensity (TBI) levels 19.63-fold higher than the CQM NPs-treated group (Fig. 6b, c). H&E staining of lung sections further confirmed the strong anti-metastatic effect of CQM NPs, revealing a 81.64% reduction in the area of pulmonary metastatic lesions compared to the control group (Fig. 6d, e), representing markedly superior therapeutic outcomes against pulmonary metastatic tumors relative to previously reported nanoparticlebased interventions [47, 48]. Ki67 and yH2AX immunohistochemical staining of lung sections from pulmonary metastases-bearing mice demonstrated that CQM NPs markedly inhibited tumor cell proliferation and induced DNA damage, supporting their potent antitumor efficacy

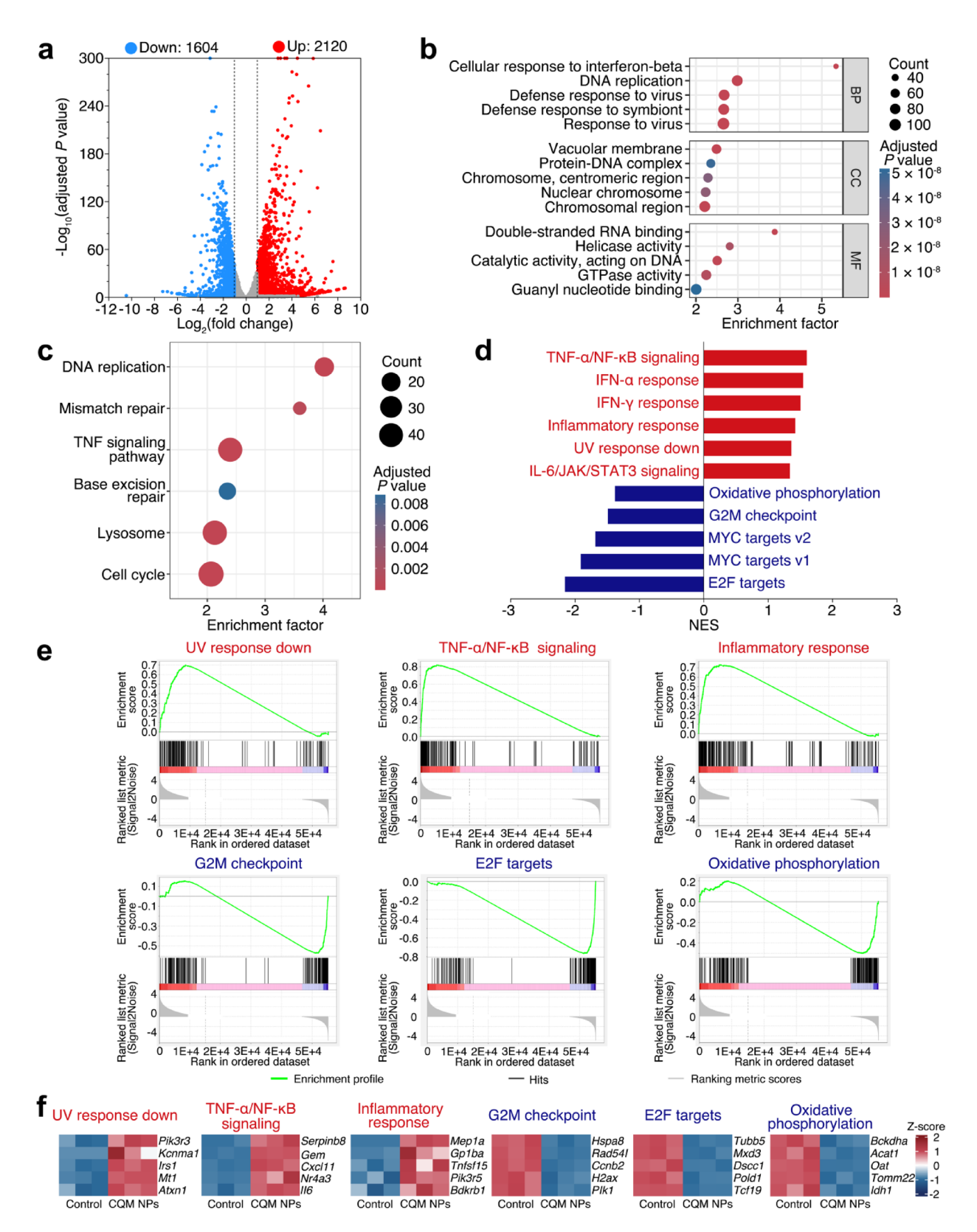


**Fig. 5** Investigation of the antitumor mechanism of CQM NPs. (a) Volcano plot of DEGs in 4T1 cells between the control and CQM NPs-treated group. (b) GO enrichment analysis of the DEGs between the control and CQM NPs-treated group. (c) KEGG pathway enrichment analysis of DEGs between the control and CQM NPs-treated group. NES, normalized enrichment score. (f) Heat maps displaying the DEGs of interest between the control and CQM NPs-treated group (n = 3 independent experiments)

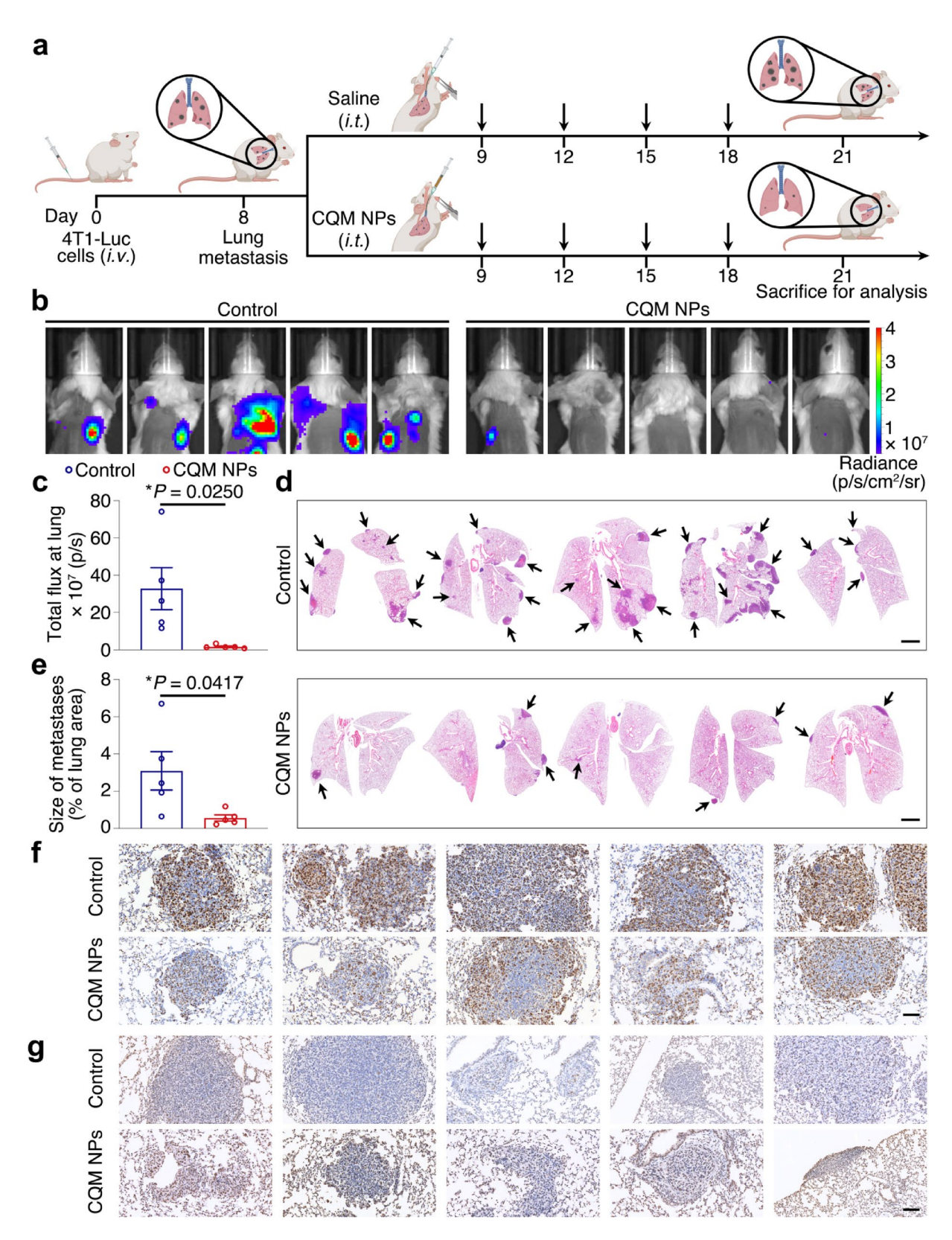


Fig. 6 (See legend on next page.)

(See figure on previous page.)

**Fig. 6** Antitumor therapy of pulmonary metastasis using *i.t.* administration of CQM NPs. (**a**) Schematic illustration of the therapeutic regimen with CQM NPs and subsequent analysis of pulmonary metastasis. The black arrows indicate *i.t.* administration. (**b**) Representative BLI images of pulmonary metastases-bearing mice in different groups. (**c**) Quantification of TBI based on BLI images. Data is represented as mean ± SEM (n=5 independent experiments). (**d**) Representative H&E-stained images of lung sections, scale bar: 2 mm. The black arrows highlight pulmonary metastatic tumor lesions. (**e**) Quantification of the area ratio of metastatic lesions to the whole lung based on H&E-stained lung sections. Data is represented as mean ± SEM (n=5 independent experiments). Immunohistochemical staining of Ki67 (**f**) and γH2AX (**g**) in lung tissues from pulmonary metastases-bearing mice in different groups, scale bar: 100 μm

(Fig. 6f, g). Moreover, the control group exhibited significant weight loss due to the progression of lung metastasis, whereas the weights of mice treated with CQM NPs remained stable throughout the study (Fig. S25). In addition to lung metastases, the control group displayed a higher incidence of tumors metastasizing to other tissues (Fig. S26). Histopathological analysis of major organs (heart, liver, spleen, and kidney) from both groups showed no noticeable abnormalities in the nuclei or cytoplasm, indicating the safety profile of CQM NPs during the anti-metastasis regimen (Fig. S27 and S28).

## Prophylactic effect of CQM NPs on pulmonary metastasis using i.t. Administration

The successful inhibition of pulmonary metastasis through *i.t.* administration of COM NPs inspired us to explore their potential as a prophylactic agent to prevent the colonization of CTCs in the lungs. Mice were intratracheally administered with CQM NPs or saline every three days. After three treatments, 4T1-Luc tumor cells were intravenously injected on day 0 to induce lung metastasis. Lung metastasis formation was then evaluated by BLI and H&E staining on day 9 (Fig. 7a). The results showed that the TBI of the lungs of CQM NPs-treated mice was only 10.81% of that in the control group, and the number of metastatic lesions was reduced by 78.08% compared to the control group (Fig. 7b-e). The prophylactic efficacy of CQM NPs surpasses existing nanotherapies for pulmonary metastatic tumors documented in prior study [49]. Consistent with its therapeutic effects, Ki67 and yH2AX immunohistochemical staining revealed significant antiproliferative activity and DNA damage in lung tissue (Fig. 7f, g). The treatment of CQM NPs contributed to a significant elevation of survival rates compared to the control group (Fig. S29). Additionally, no significant weight loss or histopathological abnormalities in the nuclei or cytoplasm of major organs (heart, liver, spleen, and kidney) were observed in either group during the prophylactic regimen (Figs. S30-S32). Blood tests and biochemical parameters also remained within normal ranges for both groups (Tables. S5-S8), further confirming the physiological safety of CQM NPs-based therapy.

#### Discussion

Firstly, to our knowledge, this is the first report of a metastasis-targeted NP theranostic system achieved by sequential macrophage reprograming after phagocytosis. Notably, we observed significant CQM NPs accumulation at pulmonary metastases following *i.t.* administration as well (Fig. S33), indicating that CQM NPs can also stimulate and polarize lung macrophages towards an M2 phenotype, which facilitates tumor targeting. Given the widespread distribution of macrophages in vivo, this strategy could be broadly applicable to the targeted delivery of other NPs or biomacromolecules across various administration routes. Additionally, incorporating quercetin (or other M2 inducers) as an excipient may further improve the targeting performance of conventional delivery systems.

Secondly, while M2 macrophages deliver their cargo to the periphery of tumor lesions, deeper penetration into the tumor depends on transcellular transport. Our observations suggest that transcellular transport of hitch-hiked NPs was achieved by vesicles-mediated delivery. Although we observed and successfully collected vesicles involved in CQM NPs transfer, the underlying mechanisms require further exploration. Specifically, the mechanisms of exocytosis of NPs from macrophages and subsequently their endocytosis of the NPs by cancer cells, as well as whether the dual TME-responsive function of CQM NPs contributes to the transcellular transportation, remain to be explored.

Thirdly, during the first 3 h post-phagocytosis, the M2-dominant phenotype facilitates navigation to the tumor sites. It is important to note that, from an antitumor perspective, promoting macrophage polarization toward the M2 phenotype should typically be avoided, as this state can support primary tumor metastasis. However, this polarization subsequently attenuates and reverses toward the M1 phenotype upon delivery to the tumor cells, triggering pro-inflammatory responses that promote tumor cell death, which results in robust therapeutic and prophylactic effects in pulmonary metastasis models treated with CQM NPs. It underscores the pivotal role of the optimal timing of macrophage phenotypic switching in achieving theranostic purposes in pulmonary metastasis.

Finally, these findings not only provide immediate solutions for pulmonary metastasis management, but also open new possibilities for treating other aggressive cancers where immune microenvironment modulation is crucial. Future work should explore the platform's adaptability to different cancer types and combination therapies. More fundamentally, our results suggest that

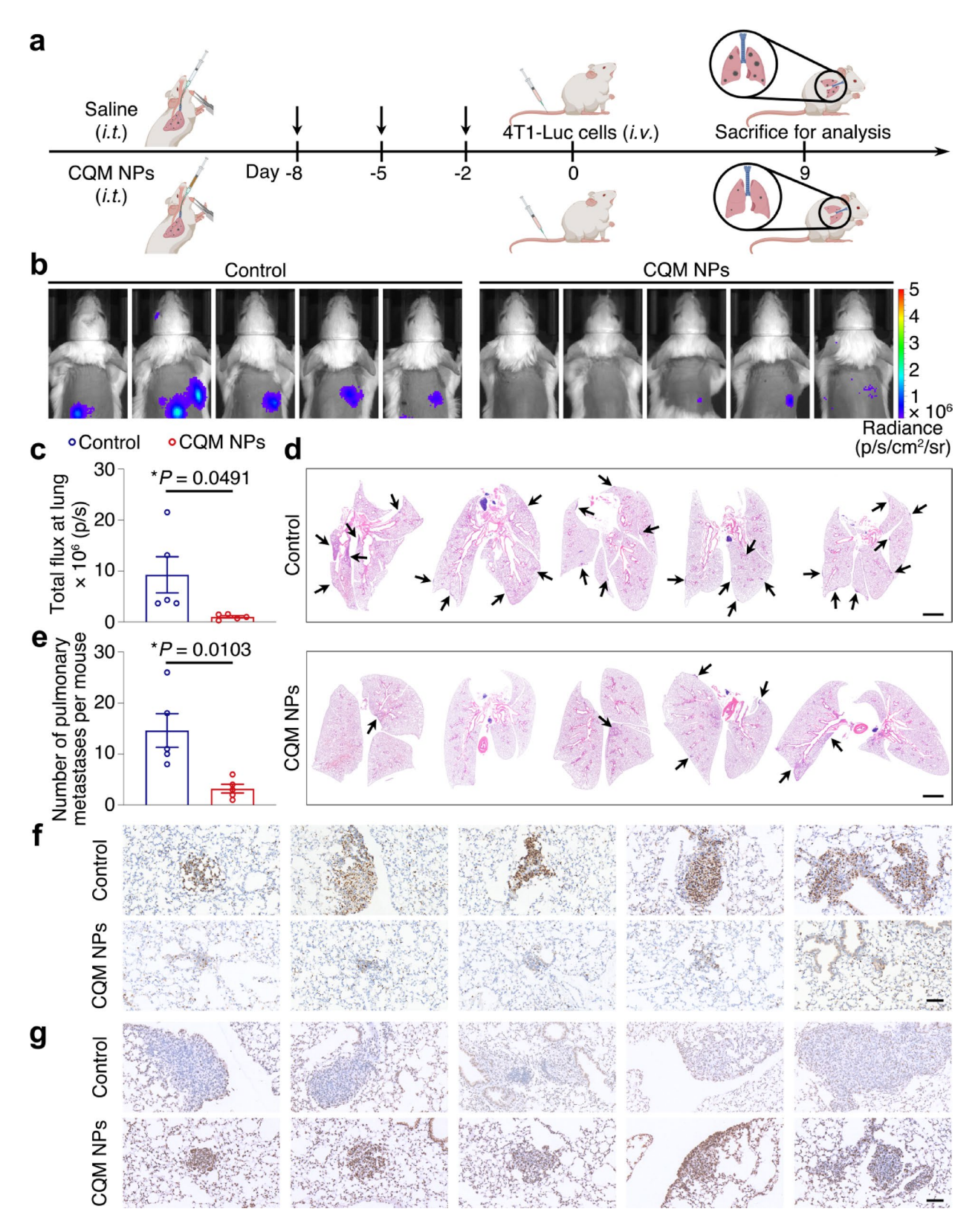


Fig. 7 (See legend on next page.)

(See figure on previous page.)

Fig. 7 Prophylactic effect of CQM NPs on pulmonary metastasis using i.t. administration. (a) Schematic illustration of the prophylactic regimen and subsequent analysis of pulmonary metastasis following CQM NPs treatment. The black arrows indicate i.t. administration. (b) Representative BLI images of mice in different groups. (c) Quantification of TBI based on BLI images. Data is represented as mean  $\pm$  SEM (n=5 independent experiments). (d) Representative H&E-stained images of lung sections, scale bar: 2 mm. The black arrows highlight pulmonary metastatic tumor lesions. (e) Quantification of the number of metastatic lesions based on H&E-stained lung sections. Data is represented as mean  $\pm$  SEM (n=5 independent experiments). Immunohistochemical staining of Ki67 (f) and  $\gamma$ H2AX (g) in lung tissues from mice intravenously injected with 4T1-Luc tumor cells following different treatments, scale bar: 100  $\mu$ m

leveraging the dynamic nature of biological systems, rather than working against them, may represent a general strategy for developing next-generation theranostics. This paradigm could transform approaches to metastatic disease by integrating diagnosis, prevention and treatment into a single coordinated intervention.

#### **Conclusions**

In conclusion, we have successfully developed core-shell structured CQM NPs for MRI detection and treatment of ultrasmall pulmonary metastases. The CQM NPs demonstrate exceptional  $T_1$ -weighted contrast enhancement when in response to the TME, establishing them as a highly sensitive MRI contrast agent. Additionally, after phagocytosis, CQM NPs can be guided to metastatic tumor sites by M2 macrophages. They also show strong inhibitory and prophylactic effects against metastatic lung tumors. Together, these attributes position CQM NPs as a promising MRI contrast agent for early detection and a potential therapeutic option for pulmonary metastasis, offering hope for reducing the high mortality associated with this devastating disease.

#### **Abbreviations**

2-DG	2-deoxy-D-glucose
ANOVA	Analysis of variance

Bio-TEM Bio-transmission electron microscopy

BP Biological processes
CA Contrast agent
CAs Contrast agents
CC Cellular components
CCK-8 Cell Counting Kit-8

CDM NPs CaCO<sub>3</sub>@dopamine-Mn nanoparticles

CNPs CaCO<sub>3</sub> nanoparticles

CQM NPs CaCO<sub>3</sub>@quercetin-Mn nanoparticles

CTCs Circulating tumor cells
Cy5 Sulfo-Cyanine 5
Cy5@CQM NPs
DAPI Sulfo-Cyanine 5@CQM NPs
4/6-diamidino-2-phenylinde

DAPI 4,6-diamidino-2-phenylindole
DEGs Differentially expressed genes
DLS Dynamic light scattering

DMEM Dulbecco's Modified Eagle Medium
DPBS Dulbecco's phosphate-buffered saline
DTNB 5,5'-dithiobis(2-nitrobenzoic acid)

FBS Fetal bovine serum
FCM Flow cytometry
FDR False discovery rate
GO Gene Ontology
GPx Glutathione peroxidase
GSEA Gene Set Enrichment Analysis

GSH Glutathione

ICP-MS Inductively coupled plasma mass spectrometer

i.t. Intratracheal i.v. Intravenous

KEGG Kyoto Encyclopedia of Genes and Genomes

MF	Molecular functions
MRI	Magnetic resonance imaging

NPs Nanoparticles
•OH Hydroxyl radical

PBS Phosphate-buffered saline
PCA Principal component analysis
PDI Polydispersity index
Pen-Strep Penicillin-streptomycin

p.i. Post injection POD Peroxidase

PQM NPs Polystyrene@quercetin-Mn nanoparticles

QM Quercetin-Mn

RES Reticuloendothelial system
SEM Standard error of mean
SPF Specific pathogen-free
TAMs Tumor-associated macrophages
TBI Total bioluminescence intensity.

TBI Total bioluminescence intensity
TBR Tumor-to-background ratio

TE Echo Time

TEM Transmission electron microscopy
TMB 3,3',5,5'-tetramethylbenzidine
TME Tumor microenvironment

TR Repetition Time

t-SNE t-distributed stochastic neighbor embedding

UV-vis Ultraviolet-visible

XPS X-ray photoelectron spectroscopy

#### **Supplementary Information**

The online version contains supplementary material available at https://doi.org/10.1186/s12951-025-03749-5.

Supplementary Material 1

#### Acknowledgements

The authors thank the Core Facility of Wuhan University for providing the inductively coupled plasma-mass spectrometry tests.

#### **Author contributions**

Xin Zhou and Daiqin Chen conceived the study. Xin Zhou, Shizhen Chen and Daiqin Chen supervised the project. Daiqin Chen and Meiju Sui performed the experiments and analyzed the data. Yingying Luo conducted the antitumor mechanism analysis. Haiqiang Wang, Hao Sheng and Meiju Sui carried out the animal studies. Sen Yue, Xiaoxun Liu and Sha Li contributed to the design and execution of the cell-based assays. Daiqin Chen, Kairu Xie and Meiju Sui prepared the figures. Daiqin Chen and Meiju Sui wrote the original draft. Daiqin Chen, Jung Soo Suk, Hao Sheng and Meiju Sui reviewed and edited the manuscript.

#### **Funding**

This work was financially supported by the National Natural Science Foundation of China (22374157, U21A20392, 82127802), Strategic Priority Research Program of the Chinese Academy of Sciences (XDB0540000, XDC0170000), Key Research Program of Frontier Sciences, CAS (ZDBS-LY-JSC004), Hubei Provincial Key Technology Foundation of China (2021ACA013) and Major Program (JD) of Hubei Province (2023BAA021).

#### Data availability

The datasets used and/or analyzed during the current study are available from the corresponding author on reasonable request.

#### **Declarations**

#### Ethics approval and consent to participate

All animal procedures were performed under the guidelines of the Animal Welfare and Research Ethics Committee at the Innovation Academy for Precision Measurement Science and Technology, Chinese Academy of Sciences (APM21018T).

#### Consent for publication

Not applicable.

#### Competing interests

The authors declare no competing interests.

#### **Author details**

<sup>1</sup> State Key Laboratory of Magnetic Resonance Spectroscopy and Imaging, National Center for Magnetic Resonance in Wuhan, Wuhan Institute of Physics and Mathematics, Innovation Academy for Precision Measurement Science and Technology, Chinese Academy of Sciences, Wuhan 430071, P. R. China

<sup>2</sup>University of Chinese Academy of Sciences, Beijing 100049, P. R. China <sup>3</sup>Department of Neurosurgery and Medicine Institute for Neuroscience Discovery (UM-MIND), University of Maryland School of Medicine, 670 West Baltimore Street, HSR III Rm 9106, Baltimore MD 21201, USA <sup>4</sup>Key Laboratory of Biomedical Engineering of Hainan Province, School of Biomedical Engineering, Hainan University, Haikou 570228, P. R. China

Received: 18 August 2025 / Accepted: 26 September 2025 Published online: 14 October 2025

#### References

- Siegel RL, Kratzer TB, Giaquinto AN, Sung H, Jemal A. Cancer statistics, 2025. CA Cancer J Clin. 2025;75:10–45.
- Siegel RL, Miller KD, Fuchs HE, Jemal A. Cancer statistics. CA Cancer J Clin. 2022;2022(72):7–33.
- Schroeder A, Heller DA, Winslow MM, Dahlman JE, Pratt GW, Langer R, et al. Treating metastatic cancer with nanotechnology. Nat Rev Cancer. 2011;12:39–50.
- Crosby D, Bhatia S, Brindle KM, Coussens LM, Dive C, Emberton M, et al. Early detection of cancer. Science. 2022;375:eaay9040.
- Fitzgerald RC, Antoniou AC, Fruk L, Rosenfeld N. The future of early cancer detection. Nat Med. 2022;28:666–77.
- Branca RT, Cleveland ZI, Fubara B, Kumar CSSR, Maronpot RR, Leuschner C, et al. Molecular MRI for sensitive and specific detection of lung metastases. Proc Natl Acad Sci USA. 2010;107:3693–7.
- Lauenstein TC. Whole-body magnetic resonance imaging in patients with metastases. In: Hayat MA, editor. Cancer imaging. Amsterdam: Academic; 2008, pp. 155–60.
- Mehrabian H, Detsky J, Soliman H, Sahgal A, Stanisz GJ. Advanced magnetic resonance imaging techniques in management of brain metastases. Front Oncol. 2019;9:440.
- Lin L, Wang LV. The emerging role of photoacoustic imaging in clinical oncology. Nat Rev Clin Oncol. 2022;19:365–84.
- Chang K, Xiao L, Fan Y, Gu J, Wang Y, Yang J, et al. Lighting up metastasis process before formation of secondary tumor by phosphorescence imaging. Sci Adv. 2023;9:eadf6757.
- Fortuin A, Rooij MD, Zamecnik P, Haberkorn U, Barentsz J. Molecular and functional imaging for detection of lymph node metastases in prostate cancer. Int J Mol Sci. 2013;14:13842–75.
- Hengerer A, Grimm J. Molecular magnetic resonance imaging. Biomed Imaging Interv J. 2006;2:e8.
- 13. Lu Z, Laney V, Li Y. Targeted contrast agents for magnetic resonance molecular imaging of cancer. Acc Chem Res. 2022;55:2833–47.
- Ersoy H, Rybicki F, Prince M. Contrast agents for cardiovascular MRI. In: Kwong RY, editor. Cardiovascular magnetic resonance imaging. Contemporary Cardiology: Humana; 2008. pp. 237–54.
- Cheng W, Ping Y, Zhang Y, Chuang K, Liu Y. Magnetic resonance imaging (MRI) contrast agents for tumor diagnosis. J Healthc Eng. 2013;4:23–45.
- Janib SM, Moses AS, MacKay JA. Imaging and drug delivery using theranostic nanoparticles. Adv Drug Deliv Rev. 2010;62:1052–63.

- 17. Lu H, Chen A, Zhang X, Wei Z, Cao R, Zhu Y, et al. A ph-responsive  $T_1$ - $T_2$  dual-modal MRI contrast agent for cancer imaging. Nat Commun. 2022;13:7948.
- Yi Z, Luo Z, Barth ND, Meng X, Liu H, Bu W, et al. In vivo tumor visualization through MRI off-on switching of NaGdF<sub>4</sub>-CaCO<sub>3</sub> nanoconjugates. Adv Mater. 2019;31:e1901851.
- Sun Z, Wang T, Wang J, Xu J, Shen T, Zhang T, et al. Self-propelled Janus nanocatalytic robots guided by magnetic resonance imaging for enhanced tumor penetration and therapy. J Am Chem Soc. 2023;145:11019–32.
- Li S, Zhan Y, Ho S, Li B, Wang M, Deng X, et al. Combination of tumorinfarction therapy and chemotherapy via the co-delivery of doxorubicin and thrombin encapsulated in tumor-targeted nanoparticles. Nat Biomedical Eng. 2020;4:732–42.
- 21. Mi P, Kokuryo D, Cabral H, Wu H, Terada Y, Saga T, et al. A pH-activatable nanoparticle with signal-amplification capabilities for non-invasive imaging of tumor malignancy. Nat Nanotechnol. 2016;11:724–30.
- Yu M, Zheng J. Clearance pathways and tumor targeting of imaging nanoparticles. ACS Nano. 2015;9:6655–74.
- 23. Feng Q, Liu Y, Huang J, Chen K, Huang J, Xiao K. Uptake, distribution, clearance, and toxicity of iron oxide nanoparticles with different sizes and coatings. Sci Rep. 2018;8:2082.
- Xu J, Ding L, Mei J, Hu Y, Kong X, Dai S, et al. Dual roles and therapeutic targeting of tumor-associated macrophages in tumor microenvironments. Signal Transduct Target Ther. 2025;10:268.
- Li S, Hou H, Chu X, Zhu Y, Zhang Y, Duan M, et al. Nanomaterials-involved tumor-associated macrophages' reprogramming for antitumor therapy. ACS Nano. 2024;18:7769–95.
- Lu Q, Chen R, Zeng F, Liu Z, Pan Y, Gao Y, et al. Inhalation of bioorthogonal gene-editable spiky-pollen reprograms tumor-associated macrophages for lung cancer immunotherapy. Adv Funct Mater. 2024;34:2408767.
- Hao N, Lü M, Fan Y, Cao Y, Zhang Z, Yang S. Macrophages in tumor microenvironments and the progression of tumors. Clin Dev Immunol. 2012;2012;948098.
- Zanganeh S, Hutter G, Spitler R, Lenkov O, Mahmoudi M, Shaw A, et al. Iron oxide nanoparticles inhibit tumor growth by inducing pro-inflammatory macrophage polarization in tumor tissues. Nat Nanotechnol. 2016;11:986–94.
- Reichel D, Tripathi M, Perez JM. Biological effects of nanoparticles on macrophage polarization in the tumor microenvironment. Nanotheranostics. 2019;3:66–88
- Wang X, Li Y, Pu X, Liu G, Qin H, Wan W, et al. Macrophage-related therapeutic strategies: regulation of phenotypic switching and construction of drug delivery systems. Pharmacol Res. 2024;199:107022.
- 31. Bui I, Bonavida B. Polarization of M2 tumor-associated macrophages (TAMs) in cancer immunotherapy. Crit Rev Oncog. 2024;29:75–95.
- 32. Lu Q, Kou D, Lou S, Ashrafizadeh M, Aref AR, Canadas I, et al. Nanoparticles in tumor microenvironment remodeling and cancer immunotherapy. J Hematol Oncol. 2024;17:16.
- 33. Pan D, Schmieder AH, Wickline SA, Lanza GM. Manganese-based MRI contrast agents: past, present, and future. Tetrahedron. 2011;67:8431–44.
- Shokrollahi H. Contrast agents for MRI. Materials Science and Engineering: C. 2013;33:4485–97.
- 35. Tsai C, Chen G, Chen Y, Shen C, Lu D, Yang L, et al. Regulatory effects of Quercetin on M1/M2 macrophage polarization and oxidative/antioxidative balance. Nutrients. 2021;14:67.
- Sun Y, Zuo Z, Kuang Y. An emerging target in the battle against osteoarthritis: macrophage polarization. Int J Mol Sci. 2020;21:8513.
- Sun Y, Wu L, Zhong Y, Zhou K, Hou Y, Wang Z, et al. Single-cell landscape of the ecosystem in early-relapse hepatocellular carcinoma. Cell. 2021;184:404–e42116.
- 88. Tan J, Wang B, Zhu L. Hydrolytic cleavage of DNA by Quercetin manganese (II) complexes. Colloids Surf B Biointerfaces. 2007;55:149–52.
- Dong Z, Feng L, Zhu W, Sun X, Gao M, Zhao H, et al. CaCO<sub>3</sub> nanoparticles as an ultra-sensitive tumor-pH-responsive nanoplatform enabling real-time drug release monitoring and cancer combination therapy. Biomaterials. 2016;110:60–70.
- Yang G, Xu L, Chao Y, Xu J, Sun X, Wu Y, et al. Hollow MnO<sub>2</sub> as a tumor-microenvironment-responsive biodegradable nano-platform for combination therapy favoring antitumor immune responses. Nat Commun. 2017;8:902.
- 41. Tang M, Zhang Z, Sun T, Li B, Wu Z. Manganese-based nanozymes: preparation, catalytic mechanisms, and biomedical applications. Adv Healthc Mater. 2022:11:e2201733.

- 42. Ma X, He C, Wang Y, Cao X, Jin Z, Ge Y, et al. Mechanisms and applications of manganese-based nanomaterials in tumor diagnosis and therapy. Biomater Res. 2025;29:0158.
- 43. Li Y, Zhao X, Liu X, Cheng K, Han X, Zhang Y, et al. A bioinspired nanoprobe with multilevel responsive *T*<sub>1</sub>-weighted MR signal-amplification illuminates ultrasmall metastases. Adv Mater. 2020;32:e1906799.
- 44. Briukhovetska D, Dörr J, Endres S, Libby P, Dinarello CA, Kobold S. Interleukins in cancer: from biology to therapy. Nat Rev Cancer. 2021;21:481–99.
- 45. Wen E, Tian Y, Chen Y, Wang Z, Feng Y, Liao Z. Tumor microenvironment responsive Mn-based nanoplatform activate cGAS-STING pathway combined with metabolic interference for enhanced anti-tumor therapy. J Nanobiotechnol. 2025;23:377.
- Luo R, Li X, Zhang M, Huang D, Le H, He T, et al. An asynchronous-regulated nanosheet cascade amplifies sonodynamic-triggered self-enhanced DNA damage for intensive tumor immunotherapy. ACS Nano. 2025;19:25552–65.
- 47. Jiang R, Li L, Li M. Biomimetic construction of degradable DNAzyme-loaded nanocapsules for self-sufficient gene therapy of pulmonary metastatic breast cancer. ACS Nano. 2023;17:22129–44.

- Naidu GS, Rampado R, Sharma P, Ezra A, Kundoor GR, Breier D, et al. Ionizable lipids with optimized linkers enable lung-specific, lipid nanoparticlemediated mRNA delivery for treatment of metastatic lung tumors. ACS Nano. 2025;19:6571–87.
- Oltmanns F, Antão AV, Irrgang P, Viherlehto V, Jörg L, Schmidt A, et al. Mucosal tumor vaccination delivering endogenous tumor antigens protects against pulmonary breast cancer metastases. J Immunother Cancer. 2024;12:e008652.

#### Publisher's note

Springer Nature remains neutral with regard to jurisdictional claims in published maps and institutional affiliations.